The MICOS Complex Regulates Mitochondrial Structure and Oxidative Stress During Age-Dependent Structural Deficits in the Kidney

Zer Vue[1*], Praveena Prasad[2*], Han Le[1*], Kit Neikirk[1], Chanel Harris[1], Edgar Garza-Lopez[3], Eric Wang[4], Alexandria Murphy[2], Brenita Jenkins[2], Larry Vang[1], Estevão Scudese[1], Bryanna Shao[1], Ashlesha Kadam[5], Jianqiang Shao[6], Andrea G. Marshall[1], Amber Crabtree[1], Benjamin Kirk[3], Alice Koh[1], Genesis Wilson[1], Ashton Oliver[1], Taylor Rodman[1], Kinuthia Kabugi[1], Ho-Jin Koh[7], Quinton Smith[4], Elma Zaganjor[1], Celestine N. Wanjalla[8], Chandravanu Dash[9], Chantell Evans[10], Mark A. Phillips[11], David Hubert[11], Olujimi Ajijola[12], Aaron Whiteside[13], Young Do Koo[3,14], André Kinder[15], Mert Demirci[8], Claude F. Albritton[8,16], Nelson Wandira[8], Sydney Jamison[8], Taseer Ahmed[8], Mohammad Saleem[8], Dhanendra Tomar[5], Clintoria R. Williams[13], Mariya T. Sweetwyne[17], Sandra A. Murray[18], Anthonya Cooper[18], Annet Kirabo[8,19,20,21], Pooja Jadiya[22], Anita Quintana[23], Prasanna Katti[24,25], Dao□Fu Dai[26], Melanie R. McReynolds[#2], Antentor Hinton, Jr[#1]

Affiliations:

1. Department of Molecular Physiology and Biophysics, Vanderbilt University, Nashville, TN, 37232, USA.
2. Department of Biochemistry and Molecular Biology, The Huck Institute of the Life Sciences, Pennsylvania State University, State College, PA 16801
3. Department of Internal Medicine, University of Iowa, Iowa City, IA, 52242, USA.
4. Department of Chemical and Biomolecular Engineering, University of California, Irvine, CA, 92697, USA.
5. Department of Internal Medicine, Section of Cardiovascular Medicine, Wake Forest University School of Medicine, Winston-Salem, NC 27157 USA
6. Central Microscopy Research Facility, University of Iowa, Iowa City, IA, 52242, USA.
7. Department of Biological Sciences, Tennessee State University, Nashville, TN 37209, USA
8. Department of Medicine, Vanderbilt University Medical Center, Nashville, TN 37232
9. Department of Biochemistry, Cancer Biology, Pharmacology and Neuroscience, Meharry Medical College, Nashville, TN, United States
10. Department of Cell Biology, Duke University School of Medicine, Durham, NC, 27708, USA
11. Department of Integrative Biology, Oregon State University, Corvallis, OR, 97331, USA.
12. UCLA Cardiac Arrhythmia Center, University of California, Los Angeles, CA, USA.
13. Department of Neuroscience, Cell Biology and Physiology, Wright State University, Dayton, OH 45435 USA
14. Fraternal Order of Eagles Diabetes Research Center, Iowa City, Iowa, USA
15. Artur Sá Earp Neto University Center - UNIFASE-FMP, Petrópolis Medical School, Brazil
16. Department of Biomedical Sciences, School of Graduate Studies, Meharry Medical College, Nashville, TN 37208-3501, USA.
17. Department of Laboratory Medicine and Pathology, University of Washington, Seattle, WA, 98195, USA
18. Department of Cell Biology, School of Medicine, University of Pittsburgh, Pittsburgh, PA, 15260, USA
19. Vanderbilt Center for Immunobiology, Vanderbilt University, Nashville, TN, 37232, USA.

20. Vanderbilt Institute for Infection, Immunology and Inflammation, Vanderbilt University, Nashville, TN, 37232, USA.
21. Vanderbilt Institute for Global Health, Vanderbilt University, Nashville, TN, 37232, USA.
22. Department of Internal Medicine, Section of Gerontology and Geriatric Medicine, Sticht Center for Healthy Aging and Alzheimer's Prevention, Wake Forest University School of Medicine, Winston-Salem, NC
23. Department of Biological Sciences, Border Biomedical Research Center, The University of Texas at El Paso, El Paso, Texas, USA
24. National Heart, Lung and Blood Institute, National Institutes of Health, 9000 Rockville Pike, Bethesda, MD 20892, USA
25. Department of Biology, Indian Institute of Science Education and Research (IISER) Tirupati, AP, 517619, India
26. Department of Pathology, Johns Hopkins University School of Medicine, Baltimore, MD, USA.

*These authors share co-first authorship.
#These authors share co-senior authorship.

Corresponding Author:
Antentor Hinton
Department of Molecular Physiology and Biophysics
Vanderbilt University
antentor.o.hinton.jr@Vanderbilt.Edu 319-383-3095

ABSTRACT:

The kidney filters nutrient waste and bodily fluids from the bloodstream, in addition to secondary functions of metabolism and hormone secretion, requiring an astonishing amount of energy to maintain its functions. In kidney cells, mitochondria produce adenosine triphosphate (ATP) and help maintain kidney function. Due to aging, the efficiency of kidney functions begins to decrease. Dysfunction in mitochondria and cristae, the inner folds of mitochondria, is a hallmark of aging. Therefore, age-related kidney function decline could be due to changes in mitochondrial ultrastructure, increased reactive oxygen species (ROS), and subsequent alterations in metabolism and lipid composition. We sought to understand if there is altered mitochondrial ultrastructure, as marked by 3D morphological changes, across time in tubular kidney cells. Serial block facing-scanning electron microscope (SBF-SEM) and manual segmentation using the Amira software were used to visualize murine kidney samples during the aging process at 3 months (young) and 2 years (old). We found that 2-year mitochondria are more fragmented, compared to the 3-month, with many uniquely shaped mitochondria observed across aging, concomitant with shifts in ROS, metabolomics, and lipid homeostasis. Furthermore, we show that the mitochondrial contact site and cristae organizing system (MICOS) complex is impaired in the kidney due to aging. Disruption of the MICOS complex shows altered mitochondrial calcium uptake and calcium retention capacity, as well as generation of oxidative stress. We found significant, detrimental structural changes to aged kidney tubule mitochondria suggesting a potential mechanism underlying why kidney diseases

occur more readily with age. We hypothesize that disruption in the MICOS complex further exacerbates mitochondrial dysfunction, creating a vicious cycle of mitochondrial degradation and oxidative stress, thus impacting kidney health.

Keywords: Mitochondria; Metabolism; Kidney; 3DEM; ROS; MICOS complex

INTRODUCTION:

Kidneys are principally known for their role in the excretion of waste products, though their full functions go far beyond, including hormonal signaling, which makes the kidney critical for many other functions, such as blood pressure regulation [1]. However, dysfunction may occur in various states, such as the sudden loss of kidney function, acute kidney injury (AKI), and chronic kidney diseases (CKD) [2] of various etiologies. An estimated 90% of individuals are not aware of their AKI and CKD, thus the exact magnitude of kidney diseases remains difficult to measure [3]. However, poor treatment outcomes for kidney diseases and associations with other conditions, such as cardiovascular disease, emphasize the importance of developing new effective treatments [4]. Kidneys are among the most mitochondrial-rich tissues in the body[5], therefore one approach to expand our understanding of kidney pathological processes is the study of mitochondria's roles in kidney functions [5].

It is well established that mitochondria provide numerous critical cellular functions beyond oxidative phosphorylation[6]. Mitochondria play a role in cell signaling, calcium regulation, apoptosis, and general homeostasis. Mitochondrial genes also encode the pathways responsible for ATP generation[7]. Mitochondria dysfunction has been implicated in kidney diseases [8–11] as well as other diseases impacting mitochondrial-rich organs including muscle diseases [12,13], neurological diseases [14,15], and obesity-related diabetes [16,17]. Notably, specific mechanisms of mitochondrial dysfunction that may govern each disease state, and ways to rescue mitochondria function, remain nascent research topics. Therefore, it is important to explore the therapeutic relevance of mitochondria.

Studies have shown that mitochondrial dysfunction is one of the hallmarks of AKI pathogenesis, making mitochondria a critical target to restore kidney function to pre-disease states [2,18]. Other focus areas for kidney research include autosomal dominant polycystic kidney disease, which has been shown to shift mitochondrial function to anaerobic respiration[19], limiting oxidative capacity, through numerous mechanisms, such as calcium signaling. Mitochondrial primary roles, frequency, and connections in different tissues may vary significantly. For mitochondrial calcium regulation, the mitochondrial calcium uniporter (MCU), which regulates calcium influx in mitochondria, is more active in the kidney than in other mitochondrial-rich organs like the liver and the heart [20]. Still, the mechanisms that mediate kidney mitochondrial dynamics remain unclear.

One link between mitochondria and kidney diseases is aging. Aging is the greatest risk factor for both CKD and AKI. While mitochondrial dysfunction is a hallmark of aging [21], an increased risk of AKI and CKD is believed to be due to aging [22,23]. It is well established that mitochondria across organ systems lose peak function with aging [24–26]. Past research has implicated that in mouse kidneys, mitochondrial bioenergetics is lost due to proton leak, reducing electron transfer [27]. Furthermore, clearance of damaged mitochondria via mitophagy responses are also blunted across aging in kidney proximal tubules [28]. However, it is poorly understood how mitochondria function declines with age and the relationship between mitochondrial dysfunction and mitochondrial structure in kidneys. It is possible that similar to other models, there is decreased fusion in the mitochondria, resulting in damaged mitochondria and cristae breakdown. This was shown by previous studies looking at kidneys with age via transmission electron microscopy (TEM) [29]. However, investigating mitochondria at 2D does not provide sufficient details and subcellular structures of mitochondria [30,31]. Thus, we performed 3D reconstruction through serial block face-scanning electron microscopy, which allows for a broader analysis range [32,33], to determine how mitochondrial networking and broad structures are

altered across aging in mouse kidneys. We studied mice at two ages: 3-month mice, representing a young adult phenotype, and 2-year mice, representing a geriatric model [34].

Here, we investigated changes in the structure and physical appearance of kidneys in young and old groups. We then studied mitochondria and cristae morphological changes in both 2D and 3D, and mitochondrial reactive oxygen species (ROS) production in young and aged mice. Mitochondrial ROS synthesis mainly occurs on the electron transport chain located in the inner mitochondrial membrane during the process of oxidative phosphorylation [35,36]. Damaged or dysfunctional mitochondria are harmful to the cells because they release substances that promote cell death and create ROS which causes TEC apoptosis [36]. The relationships between mitochondrial oxidative stress, ROS production, and mitophagy are closely intertwined, and these processes are all involved in pathological conditions of AKI [36].

Past studies have suggested that dysfunction of the mitochondrial contact site and cristae organizing system (MICOS) complex, a group of proteins regulating cristae morphology, can cause oxidative stress [37]. Given that we have previously found age-dependent losses in the MICOS complex correlating with mitochondrial structural defects in skeletal muscle and cardiac tissue [38,39], we hypothesized that a similar phenotype may be observed in the kidney, which could confer oxidative damage and impaired calcium homeostasis characteristic of age-related AKI and CKD [40,41]. We found that deletion of the MICOS genes resulted in mitochondrial structural changes and impairments in mitochondrial calcium regulation in the kidney. Because we showed that aging affects both the kidneys and mitochondria structure and MICOS, we investigated the metabolomic and lipidomic changes in aging kidneys to understand further the pathways that may mediate mitochondrial and MICOS roles in aging kidney vulnerability to injury and disease.

Results:

Human Aging Causes Minimal Changes in Kidney Size

Previous studies have utilized magnetic resonance imaging of solid renal masses as a proxy for pathologic classification and defining kidney structure [42,43]. Generally, it has been found that following the age of 60, there is a reduction in kidney volume at a rate of approximately 16 cubic centimeters per decade [44]. Thus, we utilized magnetic resonance imaging to determine how the kidney is remodeled during the aging process. By enrolling female and male participants (Figures 1A–D), we created a “young” cohort (n = 14) consisting of individuals under 50 years old and an “old” cohort of individuals older than 60 years old (n = 20) (Supplemental File 1). For both sexes, the kidney area did not show a significant change (Figures 1E–F). In-phase, which refers to aligned fat and water molecules, and out-of-phase, or opposed phase, intensity were similarly minimally changed in both females and males across aging (Figures 1G-J). We did observe that the old cohort of males had a significantly reduced in-phase intensity (Figure 1H). From there, we proceeded to calculate a ratio of in-phase to out-of-phase intensity, which showed no significant differences (Figures 1K-L). When male and female subjects were combined, kidney from male and female was not significantly differentiated across the aging process (Supplemental Figure 1A). We generally observed minimal sex-dependent differences during the aging process (Supplemental Figures 1B–E). Interestingly, old females did have a significantly lower cross-sectional area than aged males, increasing a potential increased susceptibility to aging with sex-dependent differences in kidney aging (Figure 1B). While we could not confirm subjects had kidney disease, these results support a slight age-related decline

in kidney structure. However, while gross morphological changes may be minimal, we sought to further elucidate tissue changes with aging.

Murine in Aging Results in Interstitial Fibrosis and Oxidative Stress

Previous studies have shown that interstitial fibrosis on kidney biopsy is regarded as a prognostic indicator, although its effectiveness as a diagnostic marker can be mixed, generally it can represent a nephropathy [45,46]. We looked at young (4–5 months old; Figure 2A) and old (21–23 months old; Figure 2B) C57BL/6J mice with trichrome blue to stain connective tissue blue. Concurrent with previous studies [47], we found that the trichrome area percentage increased in comparing young (5.8%) and old mice (11.0%), indicating a higher degree of interstitial fibrosis (Figure 2C). From there, we used immunohistochemistry to look at nitrotyrosin, as stained in brown areas. Studies have shown that increased nitrotyrosine levels correlate with renal dysfunction and inflammatory processes, serving as a biomarker for kidney diseases such as AKI and CKD, as well as overall mortality in these disease states [48–50]. Our results showed that a significant increase in nitrotyrosine in tubular epithelial cells and podocytes of old mice, as compared to their young counterparts (Figures 2D-F). This indicates that oxidative stress occurs with aging, so we sought to understand how mitochondrial structure also changes.

Ultrastructural Analysis of TEM shows Larger Mitochondria with Poor Cristae Morphology

Previous research has indicated that aging can influence the dynamics and morphological structure of the mitochondria in the kidney [51]. To see mitochondrial and cristae structure changes across aging, we first looked at the mitochondrial and cristae TEM images in 3-month and 2-year-old mice (Figures 3A-B) tubules. Interestingly, we noticed that the area of the mitochondria increased when comparing 3-month [mean of 1.57 μm^2 ± 2.09 μm^2 standard deviation (SD)] and 2-year-old (2.54 μm^2 ± 3.33 μm^2 SD) mice (Figure 3C). Similarly, the circularity index of mitochondria increased with age between 3-month (0.746 ± 0.174 SD) and 2-year (0.813 ± 0.116 SD) mice (Figure 3D). However, the mitochondrial number did not significantly change (Figure 3E). This suggests that mitochondria have higher normalcy with aging, with more relative area for oxidative phosphorylation, but these increases may also indicate pathological swelling of mitochondria [52]. Thus, we turned our attention to cristae, the inner folds of mitochondria that regulate bioenergetics [53], which showed significant losses in structural integrity across aging in the kidney. Specifically, the number of cristae decreased consistently across aging (Figures 3A-B). We looked at cristae score, which is a qualitative ordinal scale that assigns a whole-number score from “0” to “4” representing little-to-no cristae and normal well-formed cristae, respectively [54–56]. We found that cristae underwent significant age-related defects, with 3-month samples having mostly well-formed cristae (mean cristae score of 3.44 ± 0.794 SD) while 2-year samples showing few-well-formed examples of cristae (1.71 ± 0.693 SD) (Figure 3F). To verify these findings, we performed a qualitative assessment in SBF-SEM of cristae. We noted the 3D morphology of cristae in the 3-month sample (Figure 3G) was well formed and plentiful, concurrent with our TEM findings; in contrast, 2-year samples (Figure 3H) qualitatively showed many more areas lacking cristae, and the cristae present was often scattered or limited in area.

Together, based on these findings, aging in murine kidneys results in disrupted cristae and larger mitochondria, which could be due to swelling. However, it should be noted that TEM can be limited in analyzing mitochondrial changes, beyond those of cristae structure, across the

aging process, especially in the context of capturing mitochondrial changes in volume. Thus, we shifted to using SBF-SEM to rigorously analyze mitochondrial volumetric changes.

SBF-SEM Reveals Aging Results in Reduced Mitochondrial Volume in Kidney Tissue

Based on our observations of the lack of cristae folding in aging kidney tissue, we used 3-D techniques to image kidney tissue biopsies from young (3-month-old) and aged (2-year-old) mice with SBF-SEM. With ranges of 10 µm for the x- and y-planes and 50 µm for the z-plane, SBF-SEM enables 3-D reconstruction of mitochondria with an accurate spatial resolution that cannot be seen in 2-D [32,33,57]. To elucidate the changes in intermyofibrillar mitochondria in relation to aging, we surveyed approximately 250 intermyofibrillar mitochondria from each of the four male mice (n = 4) sampled (Figure 4A) at each age time point with SBF-SEM 3-D reconstruction methods, for a total of 1702 mitochondria surveyed cumulatively across age-points. At a 10 µm by 10 µm image stack resolution, ∼300 serial section orthogonal (ortho) slices with a total imaging depth of 50 µM (Figure 4B) were manually traced at transverse intervals (Figure 4C). This allowed for 3-D reconstructions of mitochondria to be created (Figure 4D) and visualized in 3-D from various viewpoints (Figure 4E; Videos 1-2).

With these observations, we sought to determine if mitochondrial networks changed in response to aging. In Figure 5, we show representative orthoslice images of the kidney tissue at each aging point (Figures 5A-A'), the overlay of the 3-D reconstruction on orthoslice (Figures 5B-B'), and the isolated 3-D reconstruction (Figures 5C-C'), with each color representing an independent mitochondrion. We found that the median mitochondrial area did not significantly change between 3-month (mean 8.29 μm^2 ± 10.1 μm^2 SD) versus 2-year (6.46 µm ± 5.31 µm SD) cohorts, unlike our TEM findings, despite great interindividual heterogeneity (Figures 5D-D'). However, the perimeter decreased between 3-month (mean 14,328 µm ± 17,723 µm) versus 2-year (10,241 µm ± 8,273 µm SD) cohorts, which also showed less intra-individual heterogeneity, generally (Figures 5E-E'). This trend towards smaller mitochondria was reflected when we compared volume between 3-month (0.920 μm^3 ± 1.06 μm^3 SD) versus 2-year (0.741 920 μm^3 ± 0.695 μm^3 SD) cohorts (Figures 5F-F'). Compared with our previous results in cardiac and skeletal muscle, both unaged and aged kidney mitochondria exhibit a relatively larger size [39]. This also shows that while TEM was able to capture some dynamics of cristae, 3D images showed that TEM age-related increase in area was incorrect, as kidney mitochondria become smaller in mice moving from adolescence to adulthood. When mitochondrial quantifications from each mouse were compared, they showed intergroup heterogeneity, particularly with one 3-month mice consistently having larger mitochondria, along with persistent intraindividual variability (Figures 5D'-F').

To further elucidate age-related changes and characterize the mitochondrial types in each age cohort, we used mito-otyping, a method similar to karyotyping, to organize mitochondria based on their volumes to better visualize the overall mitochondrial diversity (Figure 5G). Critically, this approach revealed that there were few significant changes in morphology with only branching showing reductions. In combination, the aged kidney mitochondrial morphology resembled healthy mitochondria with a reduced size that lacks a phenotype or fragmentation. Since mitochondria showed a variety of structural changes due to aging, we turned our attention to the MICOS complex as a potential mechanistic regulator of these age-related changes.

Age-Related Loss of the MICOS Complex Causes Loss of Mitochondrial Structure in HEK293 cells.

Although it is established that the MICOS complex is critical for cristae dynamics [58,59], we have also found that it can modulate overall mitochondrial structure in aging [60], yet it is unclear how aging affects the MICOS complex in aging kidney. Thus, we looked for age-related changes in three core components of the MICOS complex: *Mitofilin* (MIC60), *Chchd3* (MIC19), and *Chchd6* (MIC25), each of which are fundamental to the formation of the MICOS complex and cristae integrity [61–64]. We also looked for changes in *Opa1*, which is epistatic to a *Mitofilin*, a component of the MICOS complex, and is also known to serve as an age-dependent regulator of mitochondrial dynamics [65]. We found that the MICOS complex mRNA expression also decreased in the kidney with age (Figures 6A-D). We found, as expected, that *Opa1* mRNA decreased by over 50% between 3 months and 2 years (Figure 6A). *Mitofilin* also decreased significantly with the largest drop in fold change of any MICOS complex component (Figure 6B). Likewise, *Chchd3* and *Chchd6* mRNA transcripts also decreased with age but slightly less than *Mitofilin* (Figure 6D). Notably, while Opa1 can be epistatic to the MICOS complex, the MICOS complex modulates cristae integrity independently of it, suggesting these changes in qPCR mRNA transcripts represent non-interconnected pathways [66]. To further understand the role of mitochondrial dynamics upon the loss of these MICOS genes, we also studied the impact of losing the MICOS complex.

Since the loss of *Opa1* triggers changes in morphology [65,67], we used it as a positive control for morphological changes. We performed siRNA deletions of *Chchd3*, *Mitofilin*, *Chchd6*, and Opa1 in immortalized human embryonic kidney cells (HEK293 cells). From there, we performed TEM in each of these conditions as compared to a control (Figure 7A-E). As expected, *Opa1* deletion led to significant decreases in mitochondria area, perimeter, and length with an inverse increase in circularity index, which was expected as a result of impaired fusion dynamics (Figures 7F-I). *Chchd3* deletion shows an even more drastic phenotype of reduced mitochondrial area, while *Chchd6* deletion shows a small decrease compared to the control and *Mitofilin* deletion demonstrates no significant differences (Figure 7F). Interestingly, *Chchd3* deletion HEK293 shows a higher perimeter and length despite its decreases in area and circularity index (Figures 7F-I). *Chchd3* KO cells had nearly completely elongated mitochondria, unlike those in *Opa1* deletion. Together this shows that while the phenotype of the MICOS complex KO is distinct from the loss of OPA1, beyond only its canonic roles in cristae integrity [59], it also can modulate mitochondrial structure. Since cristae and mitochondrial dysfunction were a hallmark change in aging kidneys, we sought to understand further functional implications of the age-dependent loss of the MICOS complex.

Knockdown of MIC60 and CHCHD6 Generates Oxidative Stress in HEK293 cells.

As previously reviewed [68], oxidative stress generated across aging can confer susceptibility to kidney pathologies with characteristics that mimic aspects of kidney aging or CKD. While oxidative stress can arise through pleiotropic mechanisms including inflammation and reduced antioxidant activity [36,68,69], free radicals can be generated through the NADPH oxidases and mitochondrial electron transport chain. Thus, we examined if loss of the MICOS complex, conferring alterations in cristae integrity, also results in dysfunction of cellular respiration processes to lead to oxidative stress. To explore this paradigm, we knocked down

Chchd6 and *Mitofilin* since they both have central roles in interacting with the SAM complex to modulate cristae integrity [70]. Intracellular total and mitochondrial ROS levels were assessed by different fluorescent dyes: MitoPY1 with high specificity for H_2O_2 (Figure 7J), MitoBright, for mitochondrial ROS, and DCFDA for generalized intracellular ROS and mitochondrial superoxide production (Figure 7K). Using microscopy-based ROS quantification, we measured increases in mitochondrial ROS levels in both *Mitofilin* and *Chchd6* deletion (Figure 7L). Antimycin A treatment was used as a positive control to validate ROS quantification. Mitofilin knockdown in 293 HEK cells showed significantly increased ROS by all fluorescent dyes, whereas only MitoBright indicating mitochondrial ROS and DCFDA, indicating general intracellular ROS as well as mitochondrial superoxide production, were significantly elevated in CHCHD6 silenced cells (Figures 7N-O). In summary, the suppression of both CHCHD6 and MIC60 resulted in the elevation of ROS, implying the MICOS complex has a role in mitochondrial ROS homeostasis.

Knockdown of MIC60 and CHCHD6 impairs mCa^{2+} handling in HEK293 cells.

Ca^{2+} influences mitochondrial cristae structure [71,72]. To elucidate MICOS core components' (MIC60 and CHCHD6) role in mitochondrial calcium (mCa^{2+}) regulation, we examined mCa^{2+} uptake and retention in HEK293 cells. Both *MITOFILIN* and *CHCHD6* deletion cells show reduced mCa^{2+} uptake (Figure 8A). Furthermore, reduced mCa^{2+} uptake correlated with early permeability transition pore opening (Figure 8B). *MITOFILIN* and *CHCHD6* deletion cells showed a significant reduction in mCa^{2+} retention capacity compared to controls (Figures 7C-D). Furthermore, we confirmed for all of these experiments that siRNA successfully reduced the protein expression of MIC60 and CHCHD6 (Figures 8E-F). These findings indicate MICOS' crucial role in maintaining physiological mCa^{2+} homeostasis, with altered MICOS complex and cristae structure rendering mitochondria susceptible to Ca^{2+} flux dysregulation and mCa^{2+}-induced cell death. Since MERCs are well understood to be modulators of calcium homeostasis dependent on tethering distances [73,74], we qualitatively examined MERCs in 3D structure in aging (Figures 8G-J; Videos 3-4). We observed in aging tissue there was generally a decrease in MERCs with a phenotype of wrappER, a shape that is commonly reported in liver [75]. Since aging confers a loss of MERCs, this suggests impaired Ca^{2+}, paralleling the dysfunction that arises with the loss of the MICOS complex. Together, these results suggested the roles of mitochondria and MICOS in aging kidneys. To further investigate the pathways that regulate mitochondrial changes, metabolomics, and lipidomic profiling was studied in the kidney.

Global metabolic and lipidomic profiling highlights dynamic changes in the aged kidney.

Following our observations of dysregulation of mitochondrial structure in aging, we sought to better understand other age-related metabolic regulators that may be associated with MICOS-mediated changes in ROS production and Ca^{2+} flux. In aging samples, we conducted comprehensive metabolomic and lipidomic profiling to understand the consequences of these morphological imbalances. The metabolomics analysis unveiled disruptions in amino acid biosynthesis, altered nucleotide metabolism, and dysregulated redox signaling in aging kidney tissues (Figures 9A-B; D-H; SFigure 2). Amino acids play a pivotal role in kidney mitochondrial function, contributing to energy production, gluconeogenesis, nitrogen metabolism, protein

synthesis, antioxidant defense, and specialized metabolic pathways within mitochondria [76]. Consequently, the altered shape and size of mitochondria with age accompany disruption to normal amino acid metabolism, prompting an exploration into whether these changes are causative or consequential in the aging process. A notable finding was the significant impact on glycine, serine, and threonine metabolism in aged kidneys (Figures 9B; D-E). These amino acids are intricately linked to mitochondrial function, contributing to one-carbon metabolism, providing substrates for energy production, and maintaining cellular homeostasis. Our findings suggest disruptions to the mitochondrial glycine cleavage system (GCS), influencing the synthesis of purines, pyrimidines, and other small molecules (Figure 9E). Additionally, threonine catabolism, contributing to acetyl-CoA production for energy through oxidative phosphorylation in the mitochondria, showed significant decreases, suggesting that altered mitochondrial morphology may disrupt energy metabolism and cellular homeostasis (Figure 9D). A noteworthy decrease in valine, leucine, and isoleucine in aged kidney tissues (Figures 9F-H) raised interest. Although the biosynthesis of these branched-chain amino acids occurs in the cytoplasm, they play crucial roles in regulating mitochondrial biogenesis, autophagy, and cellular signaling. Significant depletions in tissue NAD^+, NADP, NAM, and an increase in NADH pools were also detected, indicating an age-related imbalance of cofactors (Figures 9I-L). Together, this underscores disruptions to these metabolites could be key contributors to declining kidney health and function with age due to morphological changes.

Lipidomic profiling of young and aged kidney tissues unveiled age-related changes in both lipid classes and lipid chain lengths (Figures 10A-C). In aging kidneys, significant alterations were observed in the triglycerides oligomers (TGO), triglycerides (TG), sterols (ST), N-acylethanolamines (NAE), lyso-phosphatidyl-inositol (LPI), dihexoylceramides (Hex2Cer), dilysocariolipin (DLCL), and cardiolipin (CL) lipid classes when compared to other lipid groups (Figures 10C). We also noted significant differences in lipid chain lengths with age in the kidney, which impacts membrane integrity, fluidity, and functionality (Figures 10C). Thus, our lipidomic profiling revealed disruptions in lipid classes that contribute to both energy metabolism and the maintenance of mitochondrial membrane structure, integrity, and function. This study also sheds light on novel roles for lipid classes such as NAEs and LPIs in the context of kidney aging.

Discussion:

Structural Analysis

In the past, numerous studies have looked at kidneys across aging or disease states via TEM, which provides high-resolution 2D images [29,77,78]. While TEM is a useful technique to understand changes in cristae integrity, it cannot accurately capture many structural details of mitochondria, such as diverse structures mitochondria may adapt to depending on cellular conditions [79], and we found that TEM area findings directly contradict our findings of decreased mitochondrial volume with aging. Here we utilized SBF-SEM to perform 3D reconstruction in aged mouse kidney, which showed many novel phenotypes and losses in mitochondrial volume that were otherwise not captured by MRI or TEM methods.

We have previously used 3D reconstruction to observe aged skeletal muscle in mouse [39]. We previously observed increased fragmentation which was counteracted by increased

complexity. In aging murine kidneys, mitochondrial complexity did not undergo significant changes with aging. We did note a high rate of diverse or unique mitochondrial shapes, which may in turn confer functional implications [31,79]. In this study, we found a large amount of variation in mitochondrial shape in both 3-month and 2-year aged cohorts, which show a mix of elongated, compact, big volume, small volume, nanotunnels, donut-shaped, and branching structural phenotypes. While our previous studies in skeletal and cardiac tissue showed a dominant phenotype across aging, typically of fragmentation, mitochondria in the kidney undergo different shapes, and 3-month and 2-year samples do not present vastly different phenotypes.

One notable phenotype we observed is mitochondria donuts. We found that the 3-month samples displayed many branched forms of mitochondria with high complexity and formed within them donut-like structures. Past research utilizing 3D reconstruction in the aged brain in monkeys found a high rate of the donut mitochondria phenotype in the aged cohort, which had impaired memory function [80]. Even beyond age, samples with mitochondrial donuts, which resulted in smaller synapses, had worse memory than older cohorts that had normal mitochondria [80]. While it is established that mitochondria donuts are a hallmark of mitochondrial dysfunction [7], interestingly it seems they are differentially expressed in tissue types and correlates to each tissue's functions. It has been suggested that their increased surface area relative to volume allows for them to maintain more organelle contacts at the cost of lower ATP production [79]. It has also been found that, unlike swollen mitochondria, donut mitochondria maintain more of their internal structure and, potentially as a result, are not the target of mitophagy [81]. Since our analysis shows that more donuts occur in the younger samples, these may represent a positive phenotype in some cases. Therefore, the exact roles of donut mitochondria still remain unclear and may extend beyond what has been previously hypothesized.

Beyond changes in relative bioenergetics between mitochondrial shapes, their roles in calcium homeostasis and other biomolecular pathways deserve further research. For instance, past studies have also suggested decreasing activity of the Akt pathway, which is upstream from the mTORC pathway, as a mechanism to restore autophagy, clear out defective mitochondria, and restore biogenetics [82]. However, given that other studies have shown that donut mitochondria may not be subject to autophagic clearing of mitochondria [81], suggesting a potential reason for different relative rates of mitochondrial donuts. Additionally, research of mitochondrial aging in the kidney has found that mtDNA is more error-prone across aging, with up to a 5-fold increase in the number of point mutations and deletions [82], which may also be responsible for the alterations in the mitochondria structure we observe. Thus, the exact molecular underpinnings of these various shapes are deserving of further research.

Finally, we also found differences in the structure of mitochondria, depending on their location. Through 3D reconstruction, we found that in all the aging samples of the kidney, next to the nucleus, the mitochondria are round. The further away from the nucleus, the more unique mitochondria structures, such as large volume (increased mitochondrial function capacity), small volume, elongated (relatively greater surface area facilitates interaction with the surrounding environment), compact, nano tunnels, and donut-shaped (increased surface area for interaction) are present [31]. The change in shapes likely arises as a result of mitochondrial stress [79,83]. Whereas, the areas that are not undergoing stress, likely present typical and elongated mitochondria. Therefore, it is possible that different areas of kidney undergo stress, potentially linked to stress from filtration, while others are not as susceptible to stress as aging goes. In a previous study, we have found that mitochondria in heart retain their morphology [38]. Therefore,

there may be a similar mechanism that helps retain morphology for intracellular regions, such as perinuclear kidney mitochondria. Notably, the kidney houses at least 16 types of epithelial cells [84], and the kidney also has distinct regions including the cortex, medulla, and renal sections, which serve differing functions [85]. However, our study did not permit the differentiation of these separate regions. Thus, future studies may consider using methods such as SDS-PAGE to further differentiate kidney samples [86]. Thus, future studies may further explore this by developing ways to better separate epithelial and globular areas of kidney for SBF-SEM and seeing if there are region- or area-dependent differences across aging kidney mitochondria.

The MICOS Complex as a Master Regulator

Importantly, in translating the impact of this study to AKI and CKD, mitochondria are known to be impactors in the pathophysiology of these diseases [87]. Mitochondrial dynamics are complex and observing key regulators of mitochondrial form, and thus function, may explain changes that occur in kidney disease states. Key regulators of mitochondria include OPA1 (regulating mitochondrial fusion) and DRP1 (regulating mitochondrial fission), and they may be responsible for changes observed in the kidney. Past research has shown that in AKI there is a decrease of OPA1 expression and increased DRP1 expression, suggesting the likely fragmentation of mitochondria [2]. However, beyond models with decreased expression of DRP1 not being viable, mitochondrial fission is also important to maintain various roles including microtubule trafficking [88]. Therefore, this study sought to find other targets and changes in mitochondrial structure beyond simple alterations in fusion and fission, which is often the extent of what TEM may be able to survey, and the MICOS complex is one such compelling target.

Aging in kidneys is well-established by us and others to cause interstitial fibrosis and oxidative stress [47,89–91]. Our results suggested age-related loss of the MICOS complex leads to mitochondrial structural loss, generating oxidative stress and dysregulating calcium homeostasis. Since the MICOS complex forms across cristae junctions, understanding of the interdependency of different MICOS complex proteins is still evolving, but currently, it is understood that some integral proteins such as MIC60 (*Mitofilin*) regulate the expression of other proteins including MIC10 and MIC19 [92]. Similarly, MIC60/MIC19 (*Mitofilin/Chchd3*), unlike other MICOS complex proteins, assemble independently of cardiolipin, with MIC19 being responsible for the regulation of subcomplex distribution [59]. Past studies of the MICOS complex in the kidney have been limited, but they generally show that mitochondria-rich regions including the kidney have a high rate of MIC60 and its isoforms, with a deletion of *Mitofilin* resulting in lethal disruption of the overall complex [92]. This underscores the central role of *Mitofilin*, relative to other components of the MICOS complex, with functions that extend beyond cristae and mitochondrial dynamics to nucleoid distribution, suggesting roles in mtDNA synthesis [93]. This has been recapitulated by other studies showing that *Mitofilin* depletion decreases mtDNA transcription, resulting in impaired bioenergetics in the kidney, as previously review [61]. Notably, we saw a most marked age-related decrease in *Mitofilin*, compared with other components (Figure 6), yet *Mitofilin* also showed a less drastic mitochondrial phenotype when knocked out compared with other MICOS complex proteins (Figure 7). While structural analysis of MICOS complex knockouts is limited by only being in TEM, this underscores the importance of consideration other roles of the MICOS complex beyond its extensively reviewed and well-understood role in cristae dynamics and biogenesis [58,94].

The role of the MICOS complex in disease states remains more controversial. Generally, loss of the MICOS complex has been shown to reduce cardiac ATP levels, thus impairing tissue

integrity [95]. Studies within other tissue types, such as the liver have shown that *Chchd3* depletion results in impaired MERCs to induce fatty liver disease with SLC25A46 involvement [96]. As previously reviewed [97], the MICOS complex has thus been involved in neurodegenerative disorders, metabolic syndromes, cardiac dysfunctions, and muscle pathologies. In the kidney, as previously reviewed, impairment of *Mitofilin* has specifically been implicated in the pathophysiology of mtDNA-renal diseases, diabetic kidney disease, kidney failure, and reperfusion [61]. Interestingly, other studies have suggested a protective mechanism by the loss of the MICOS complex. It is possible that loss of the MICOS complex, despite aberrant cristae structure, is a protective factor across aging by having an unexpected, pronounced lifespan extension in *Podospora anserina* [98]. Specifically, it has been suggested that Miro-MIC60 interactions impair cellular respiration and cause oxidative stress to prevent mitophagy, thus lending increased susceptibility to Parkinson's disease and Friedreich's ataxia [99]. This underscores the need to better understand the impact of MICOS complex loss.

Notably, contrary to other studies showing that Miro-MIC60 interactions cause oxidative stress, we found that deletion of the MICOS complex components, *CHCHD6* and *MITOFILIN*, resulted in mitochondrial and cell oxidative stress. As previously reviewed [61], oxidative stress has occurred upon *MITOFILIN* deletion in some tissue types such as cardiac, but the interlinking of MICOS complex and oxidative stress remains poorly elucidated. Of relevance, within the kidney, oxidative stress mediates age-associated renal cell death and has been linked to numerous pathological conditions, as previously reviewed [68]. Since the loss of the MICOS complex is well-understood to impair bioenergetics and ATP production [60,62], our findings suggest that the closely linked process of free radical generation is also bolstered. MICOS-generated ROS may have various effects; for example, they can reduce NAD+, which we observed in our aged tissue, to cause alterations in glycolysis, TCA cycle, and oxidative phosphorylation, as previously reviewed [100]. As previously reviewed, changes in fuel availability lead to alterations in TCA metabolite levels, with downstream effects in reducing mitochondrial calcium uptake and lowering matrix Ca^{2+} levels, which in turn decreases Ca^{2+}-dependent TCA cycle enzyme activity, including pyruvate dehydrogenase and α-ketoglutarate dehydrogenase, and in some cases induce autophagy as a compensatory mechanism for changes in substrate availability [101]. Since we saw concomitantly mCa^{2+} uptake is also decreased with silencing of the MICOS complex, this suggests a vicious cycle through which ROS-dependent NAD+ and calcium-dependent TCA metabolites are lost due to the MICOS complex; however, this pathway needs to be more thoroughly explored. Alternatively, oxidative stress can cause mitochondrial permeability transition pore (mPTP) openings, which adaptively release excess ROS to maintain mitochondrial homeostasis but in pathological permeant conditions can engage in destructive ROS-dependent ROS release [102,103]. While mPTP openings can be transient, calcium-dependent lowering of membrane potential can also cause permanent openings which confer increased risk to apoptotic pathways [104], suggesting an alternative pathway through which a feedback loop may arise due to ROS generation and calcium dysregulation following silencing of proteins involved in the MICOS complex.

In murine renal tubular epithelial cells, an MCU-dependent increase in mitochondrial calcium accumulation results in oxidative stress and, ultimately, senescence [105]. This study underscores the importance of further explicating the role of MICOS in senescence and the therapies that target senescence. For example, a recent study elucidated that diminished expression of GLIS1 in age-related kidney aging models correlates with impaired mitochondrial quality control mechanisms, while increased GLIS1 interaction with PGC1-α helps maintain

mitochondrial stability, thereby suggesting GLIS1 as a potential therapeutic target for mitigating cell senescence and age-related renal fibrosis [106]. Furthermore, the roles of the MICOS complex in affecting calcium highlights the importance of investigation of other regulators of mitochondrial Ca2+ uniporter (e.g., MICU1, MCU, EMRE), some of which have recently been identified to have roles in cristae morphology [72]. While MICU1 has increasingly been shown to have a role in cristae morphology [71,72], the interconnectedness of these proteins has not yet been studied in the context of downstream effectors of the MICOS complex.

Notably, past studies have shown that nicotinamide adenine dinucleotide phosphate reduced oxidase (NOX) and its oxidative stress contributes to ER stress-induced apoptosis, contributing to renal dysfunction [107]. Similarly, NOXs have been indicated to play a role in acute kidney injury by promoting oxidative stress [35,108]. Beyond underscoring the therapeutic potential of NOXs, their interdependence with ER stress also highlights the importance of studying MERCs further. MERCs, contact sites under 50 nm which can be caused by ER stress, have previously been associated with calcium signaling and lipid metabolism, but recent research has further suggested a potential role in senescence [109]. Here, we did not comprehensively study MERCs, which are known to be implicated with the calcium homeostasis with which mitochondria engage in [110]. However, a qualitative analysis did show that wrappER forms principally in young samples (Figures 8G-H). Past studies show that rough endoplasmic reticulum may curve to closely wrapped around the mitochondria and maintain lipid homeostasis, which has been termed wrappER [111]. Thus, the lipidomic shifts we observed with aging may be possibly caused by deficient lipid flux and impaired cristae structure without wrappER. This compartment, which has numerous functions including fatty acid secretion, may be an organelle linking mitochondria and peroxisomes for overall lipid balance regulation [112]. Given calcium homeostasis dysfunction is a potential avenue of kidney disease [2], it remains important to consider in the future how calcium homeostasis is impacted across aging through MERC modulation, especially as qualitatively, less MERCs appear to exist in an aged sample.

Metabolic and Lipidomic Changes

Notably, across aging we saw changes in metabolism, which have been known to arise in part due to oxidative stress generated by the MICOS complex [refs]. Oxidative stress triggers the activation of poly(ADP-ribose) polymerase (PARP) as a DNA repair mechanism, which in turn consumes nicotinamide adenine dinucleotide (NAD+), thus NAD+ levels decreased with age in both males and females [113]. Of relevance, extracellular NAD+ triggers a pathway involving cAMP to cause an influx of influx of extracellular Ca^{2+} and subsequent superoxide and nitric oxide generation [114]. A decrease in NAD+ levels has been implicated with disruption of mitochondrial homeostasis and function to lead to diabetic kidney injury [115]. Studies using nicotinamide riboside to boost NAD+ levels have shown that it may actually impair inter-organelle communication and not restore cristae dynamics [116]. This suggests that loss of the MICOS complex may partially result in a loss of NAD+ levels which may not be easily restored.

Our metabolomic data shows impairment of Pentose Phosphate Pathway (PPP); impaired glutamine conversion to glutamate, which is required for alpha-ketoglutarate (TCA) and glutathione (GSH) biosynthesis. Elevated glutamine also activates the mTOR pathway, which has been suggested to be activated to modulate mitochondria biogenesis in the kidney and is known to be activated in the aging process[117,118]. PPP is essential to supply NADPH, which is required for the endogenous glutathione antioxidant system. NAPDH is a central co-factor of lipid and redox homeostasis [119]. PPP is also essential to supply nucleosides and nucleotides;

Depletion of nucleotides, such as Xanthine and Ribose, promotes genomic instability[120]. Additionally, our results align with existing literature on dysregulated NAD^+ metabolism in aging kidneys[121]. Significant depletions in tissue NAD^+, NADP, NAM, and an increase in NADH pools were detected, indicating an age-related imbalance of cofactors (Figures 8I-L). The decline in NAD+ is linked to a redox shift hypothesis, where more NAD+ is converted to NADH without adequate reduction back to NAD^+[122]. Our data supports this hypothesis, highlighting the importance of maintaining an adequate pool of mitochondrial NAD^+ for optimal function. Further supporting a disruption in redox balance was the detection of decreased FAD (flavin adenine dinucleotide) with age in mouse kidneys (Figure 8M). Similar to NAD(H), FAD is involved in various energy production pathways, including oxidative phosphorylation, the TCA cycle, beta-oxidation of fatty acids, and the electron transport chain. In summary, our metabolomic profiling provides evidence of disruptions to energy metabolism with age, potentially acting as either a consequence or precursor to the observed morphological phenotypes we observed in aged kidney tissues.

Our lipidomics profiling showed profound changes in lipid classes. These lipid classes play diverse and intricate roles in kidney mitochondria, participating in key cellular processes. TGOs and TGs serve as energy substrates and act as a storage form of fatty acids in kidney mitochondria [123,124]. Disruptions to these lipids can impact mitochondrial beta-oxidation, providing acetyl-CoA for energy production. Sterols contribute to the structural integrity and fluidity of mitochondrial membranes, aligning with our data and observations [125,126]. Maintaining proper membrane structure is crucial for mitochondrial function, a feature lost with age in kidney tissues. The role of NAEs in endocannabinoid signaling is recognized [127,128], but their specific function in kidney mitochondria remains unclear. Notably, changes in the NAE lipid class with age in the kidney are of special interest. Additionally, while LPIs are known signaling molecules, their exact impact on mitochondrial function in the kidney requires further investigation. Here we present two novel cases of lipid classes playing a role with age in the kidney. Hex2Cer contributes to the composition of mitochondrial membranes [129,130], supporting our observation that changes in shape and size contribute to aging in the kidney. Lastly, cardiolipins (DLCL and CL), unique phospholipids predominantly found in the inner mitochondrial membrane, are crucial for maintaining mitochondrial membrane integrity, cristae structure, and the function of respiratory chain complexes [131,132]. Changes in CL content with age support the observed decline in mitochondrial stability and function of our samples.

Conclusion

Together, our results underscore that the aging of murine kidney tissue causes cristae disarray and impaired mitochondrial structure with smaller volumes. This happens alongside wide-spread metabolic and lipidomic shifts, as well as increased fibrosis and oxidative stress, which cumulatively confer decreased oxidative capacity and increased risk of age-related disease states including CKD and AKI [40]. We further found that the MICOS complex is lost with kidney aging, absent of changes of other common regulators of mitochondria, and cristae morphology. While the age-dependent loss of the MICOS complex likely accounts for the loss of cristae architecture, silencing of some components of the MICOS complex in HEK cells confers a similar structure to that of aged tissue. The MICOS complex silencing further causes both oxidative stress, reflective of aged states, and reduced mitochondrial calcium uptake. It is plausible that these changes together create a vicious cycle: MICOS loss drives oxidative stress, leading to calcium-dependent TCA dysregulation and NAD^+ dysregulation, driving more

oxidative stress and mtDNA loss, leading to a reduction in MICOS complex transcripts, causing dysfunctional mitochondrial, producing more oxidative stress byproducts, leading to age-dependent disease states.

EXPERIMENTAL PROCEDURES

Animal Care and Maintenance

Per protocols previously described [38,60,133], the care and maintenance of the male C57BL/6J mice conformed to the National Institute of Health's guidelines for the use of laboratory animals. The University of Iowa's Institutional Animal Care and Use Committee (IACUC) or University of Washington IACUC approved the housing and feeding of these mice. Anesthesia was achieved using a mixture of 5% isoflurane and 95% oxygen.

Human Sample Cohort:

All human samples were obtained from Brazilian cohorts according to the CAEE (Ethics Appreciation Presentation Certificate) guidelines. Samples from young individuals were collected, and experiments were performed under CAEE number 61743916.9.0000.5281; samples from older individuals were collected under CAEE number 10429819.6.0000.5285.

Immunohistochemistry

Young (4–5 months old) and old (21–23 months old) C57BL/6J were maintained on a chow diet. Kidney slices were embedded in OCT, with section processing as previously described [47]. Nitrotyrosine (MilliporeSigma, #06□284,1:1000), and anti-mouse IgG-HRP (Abcam; ab97046) staining was performed to measure oxidative stress. Masson trichrome staining was quantified with representative images at low power from each kidney section deconvoluted and thresholded to calculate the blue area relative to the total tissue area in ImageJ.

RNA Extraction and RT-qPCR

Using TRIzol reagent (Invitrogen), total RNA was isolated from tissues and further purified with the RNeasy kit (Qiagen Inc). RNA concentration was determined by measuring absorbance at 260 nm and 280 nm using a NanoDrop 1000 spectrophotometer (NanoDrop products, Wilmington, DE, USA). Approximately 1 µg of RNA was reverse-transcribed using a High-Capacity cDNA Reverse Transcription Kit (Applied Biosciences, Carlsbad CA). Quantitative PCR (qPCR) was then performed using SYBR Green (Life Technologies, Carlsbad, CA) [16]. For qPCR, 50 ng of cDNA was loaded into each well of a 384-well plate, with the reaction carried out on an ABI Prism 7900HT system (Applied Biosystems) with the following cycle: 1 cycle at 95°C for 10 min; 40 cycles of 95°C for 15 s; 59°C for 15 s, 72°C for 30 s, and 78°C for 10 s; 1 cycle of 95°C for 15 s; 1 cycle of 60°C for 15 s; and one cycle of 95°C for 15 s. GAPDH normalization was used to present the data as fold changes. qPCR primers used were from previously published sequences [133], as detailed in Table 1.

Table 1: qPCR Primers Used

Gene	Primers	
Opa-1	Forward	5'-ACCAGGAGACTGTGTCAA-3'
	Reverse	5'-TCTTCAAATAAACGCAGAGGTG-3'
Chchd3	Forward	5'-GAAAAGAATCCAGGCCCTTCCACGCGC-3'
	Reverse	5'-CAGTGCCTAGCACTTGGCACAACCAGGAA-3'
Chchd6	Forward	5'-CTCAGCATGGACCTGGTAGGCACTGGGC-3'
	Reverse	5'-GCCTCAATTCCCACATGGAGAAAGTGGC-3'
Mitofilin	Forward	5'-CCTCCGGCAGTGTTCACCTAGTAACCCCTT-3'
	Reverse	5'-TCGCCCGTCGACCTTCAGCACTGAAAACCTAT-3'

CRISPR-Cas9 Knockouts

All cell types were infected with the following adenoviruses for gene knockouts: control CRISPR/Cas9 (sc-418922), CHCHD6 CRISPR (sc-425817), CHCHD3 CRISPR (sc-425804), and mitofilin CRISPR (sc-429376) (Santa Cruz Biotechnology, California, US), alongside appropriate guide RNAs (Table 2). The CRISPR mixture, prepared with 2.5% CRISPR/Cas9 and 2.5% RNAiMax (ThermoFisher Scientific; 13778075) in Opti-MEM (Gibco; 31985070), was incubated for 20 minutes at room temperature. Post-incubation, cells were treated with the CRISPR mixture and incubated at 37°C. Medium changes and cell washes were performed, and experiments were conducted 3 and 7 days post-infection.

Table 2: Guide RNA and Plasmids Used

Gene Name	Type of Plasmid	CAS Number
Mitofilin	CRISPR/Cas9 KO (m)	sc-429376
CHCHD6	CRISPR/Cas9 KO (m)	sc-425817
CHCHD3	CRISPR/Cas9 KO (m)	sc-425804
Control	CRISPR/Cas9 KO (m)	sc-418922

Serial Block-Face Scanning Electron Microscope (SBF-SEM) Processing of Mouse Muscle Fibers

SBF-SEM was performed according to previously defined protocols [134–136]. Anesthesia was induced in male mice using 5% isoflurane. Post skin and hair removal, the liver was treated with 2% glutaraldehyde in 100 mM phosphate buffer for 30 minutes, dissected into 1-mm³ cubes, and further fixed in a solution containing 2.5% glutaraldehyde, 1% paraformaldehyde, and 120 mM sodium cacodylate for 1 hour.

Fixation and subsequent steps collected onto formvar-coated slot grids (Pella, Redding CA), stained and imaged as previously described [134–136]. This includes tissue washing with 100 mM cacodylate buffer, incubation in a mixture of 3% potassium ferrocyanide and 2% osmium tetroxide, followed by dehydration in an ascending series of acetone concentrations. The tissues were then embedded in Epoxy Taab 812 hard resin. Sectioning and imaging of sample was performed using a VolumeScope 2 SEM (Thermo Fisher Scientific, Waltham, MA). Conventional TEM analysis was performed on 300–400 serial sections from each sample, following staining and imaging protocols. Subsequently, analyzed, via imaging was performed

under low vacuum/water vapor conditions with a starting energy of 3.0 keV and beam current of 0.10 nA. Sections of 50 nm thickness were cut allowing for imaging at 10 nm × 10 nm × 50 nm spatial resolution.

LCMS Methods for Metabolomics

Frozen kidney tissues were weighed and ground with liquid nitrogen in a cryomill (Retsch) at 25 Hz for 45 seconds, before extracting tissues 40:40:20 acetonitrile: methanol: water +0.5% FA +15% NH4HCO3[137] with a volume of 40µL solvent per 1mg of tissue, vortexed for 15 seconds, and incubated on dry ice for 10 minutes. Kidney tissue samples were then centrifuged at 16,000 g for 30 minutes. The supernatants were transferred to new Eppendorf tubes and then centrifuged again at 16,000 g for 25 minutes to remove and residual debris before analysis. Extracts were analyzed within 24 hours by liquid chromatography coupled to a mass spectrometer (LC-MS). The LC–MS method was based on hydrophilic interaction chromatography (HILIC) coupled to the Orbitrap Exploris 240 mass spectrometer (Thermo Scientific) [138]. The LC separation was performed on a XBridge BEH Amide column (2.1 x 150 mm, 3.5 μm particle size, Waters, Milford, MA). Solvent A is 95%: 5% H2O: acetonitrile with 20 mM ammonium acetate and 20mM ammonium hydroxide, and solvent B is 90%: 10% acetonitrile: H2O with 20 mM ammonium acetate and 20mM ammonium hydroxide. The gradient was 0 min, 90% B; 2 min, 90% B; 3 min, 75% B; 5 min, 75% B; 6 min, 75% B; 7 min, 75% B; 8 min, 70% B; 9 min, 70% B; 10 min, 50% B; 12 min, 50% B; 13 min, 25% B; 14min, 25% B; 16 min, 0% B; 18 min, 0% B; 20 min, 0% B; 21 min, 90% B; 25 min, 90% B. The following parameters were maintained during the LC analysis: flow rate 150 mL/min, column temperature 25 °C, injection volume 5 µL and autosampler temperature was 5 °C. For the detection of metabolites, the mass spectrometer was operated in both negative and positive ion mode. The following parameters were maintained during the MS analysis: resolution of 180,000 at m/z 200, automatic gain control (AGC) target at 3e6, maximum injection time of 30 ms and scan range of m/z 70-1000. Raw LC/MS data were converted to mzXML format using the command line "msconvert" utility [139]. Data were analyzed via the EL-MAVEN software version 12.

LCMS Methods for Lipidomic Profiling

Kidney tissues were homogenized using a Retsch CryoMill. The homogenate was mixed with 1 mL of Extraction Buffer containing IPA/H2O/Ethyl Acetate (30:10:60, v/v/v) and Avanti Lipidomix Internal Standard (diluted 1:1000) (Avanti Polar Lipids, Inc. Alabaster, AL). Samples were vortexed and transferred to bead mill tubes for homogenization using a VWR Bead Mill at 6000 g for 30 seconds, repeated twice. The samples were then sonicated for 5 minutes and centrifuged at 15,000 g for 5 minutes at 4°C. The upper phase was transferred to a new tube and kept at 4°C. To re-extract the tissues, another 1 mL of Extraction Buffer (30:10:60, v/v/v) was added to the tissue pellet-containing tube. The samples were vortexed, homogenized, sonicated, and centrifuged as described earlier. The supernatants from both extractions were combined, and the organic phase was dried under liquid nitrogen gas. The dried samples were reconstituted in 300 µL of Solvent A (IPA/ACN/H2O, 45:35:20, v/v/v). After brief vortexing, the samples were sonicated for 7 minutes and centrifuged at 15,000 g for 10 minutes at 4°C. The supernatants were transferred to clean tubes and centrifuged again for 5 minutes at 15,000 g at 4°C to remove any remaining particulates. For LC-MS lipidomic analysis, 60 µL of the sample extracts were transferred to mass spectrometry vials. Sample analysis was performed within 36 hours after extraction using a Vanquish UHPLC system coupled with an Orbitrap Exploris 240™ mass spectrometer equipped with a H-ESI™ ion source (all Thermo Fisher Scientific). A Waters

(Milford, MA) CSH C18 column (1.0 × 150 mm × 1.7 µm particle size) was used. Solvent A consisted of ACN:H2O (60:40; v/v) with 10 mM Ammonium formate and 0.1% formic acid, while solvent B contained IPA:ACN (95:5; v/v) with 10 mM Ammonium formate and 0.1% formic acid. The mobile phase flow rate was set at 0.11 mL/min, and the column temperature was maintained at 65 °C. The gradient for solvent B was as follows: 0 min 15% (B), 0–2 min 30% (B), 2–2.5 min 48% (B), 2.5–11 min 82% (B), 11–11.01 min 99% (B), 11.01–12.95 min 99% (B), 12.95–13 min 15% (B), and 13–15 min 15% (B). Ion source spray voltages were set at 4,000 V and 3,000 V in positive and negative mode, respectively. Full scan mass spectrometry was conducted with a scan range from 200 to 1000 m/z, and AcquireX mode was utilized with a stepped collision energy of 30% with a 5% spread for fragment ion MS/MS scan.

Quantification of TEM Micrographs and Parameters Using ImageJ

Samples were fixed in a manner to avoid any bias, per established protocols [136]. Following preparation, tissue was embedded in 100% Embed 812/Araldite resin with polymerization at 60 °C overnight. After ultrathin sections (90–100 nm) were collected, they were post-stained with lead citrate and imaged (JEOL 1400+ at 80 kV, equipped with a GatanOrius 832 camera). The National Institutes of Health (NIH) *ImageJ* software was used for quantification of TEM images, as described previously [55,140].

Segmentation and Quantification of 3D SBF-SEM Images Using Amira

SBF-SEM images were manually segmented in Amira to perform 3D reconstruction, as described previously [38,39,134,140]. 300-400 slices were used and analyzed by a blind individual. 250 total mitochondria across from 3 mice were collected for each quantification. For 3D reconstruction of cardiomyocytes, 10 cells and a total of about 200 mitochondria. Quantification of 3D structures was performed using the Amira software with built-in parameters or previously described measurements [134].

Assessment of ROS levels

HEK293 WT cells (0.2 millions) were plated in 35 mm dishes. The next day, MIC60 (ThermoFisher, 136128) and CHCHD6 (ThermoFisher, 34035) siRNAs were transfected into HEK293 cells using Lipofectamine RNAiMax (Invitrogen) according to the manufacturing instructions. After incubation for 30 hrs, cells were co-stained for 30 min at 37°C with two different dyes for ROS detection: MitoBright ROS Deep Red (10 µM, Dojindo Laboratories) for mitochondrial superoxide detection, and DCFDA (10 µM, Invitrogen) for intracellular total ROS detection. Following the incubation with staining dyes, cells were washed thrice with 1X HBSS and ROS imaging was done using a confocal microscope (FV4000, Olympus Life Science).

For mitochondrial H_2O_2 imaging, cells were incubated with MitoPY1 (5 µM, Bio-Techne) for 45 min at 37°C. Cells were then washed with 1x HBSS and imaged using a confocal microscope (FV4000, Olympus Life Science). ImageJ was used for the quantification of fluorescence intensities.

Mitochondrial Intracellular Calcium

Knockdown of MIC60 and CHCHD6 in HEK293 cells.

The MIC60 and CHCHD6 siRNAs along with scramble siRNA control were transfected into HEK293 cells using Lipofectamine RNAiMax (Invitrogen) according to the manufacturer's instructions. After incubation of 48 hrs, cells were used for Calcium measurements.

Measurement of mitochondrial Ca^{2+} uptake in HEK293 cells.

Mitochondrial Ca^{2+} uptake was assessed using a multi-wavelength excitation dual-wavelength emission fluorimeter (Delta RAM, Photon Technology Int.) with slight modifications following the protocol outlined in Tomar et al., 2016 (PMID: 27184846). An equal number of cells ($2.5x10^6$ cells) were uniformly cleansed with Ca^{2+}/Mg^{2+}-free DPBS (GIBCO) and subsequently permeabilized in 1 mL of intracellular medium (ICM- 120 mM KCl, 10 mM NaCl, 1 mM KH_2PO_4, 20 mM HEPES-Tris, pH 7.2) containing 20 μg/ml digitonin, 1.5 μM thapsigargin to inhibit the SERCA pump and 2.5 mM succinate to energize the mitochondria. The loading of Fura-FF (1 μM) at the 0 s time point facilitated the measurement of mitochondrial Ca^{2+} uptake. Fluorescence was recorded at the 340- and 380-nm ex/510-nm em, with continuous stirring at 37°C, and at specified time points a bolus of 5 μM Ca^{2+} and the mitochondrial uncoupler FCCP (10 μM) were introduced in the cell suspension.

Assessment of mCa^{2+} retention capacity (CRC).

To assess mCa2+ retention capacity (CRC), 2 × 106 cells were resuspended in an intracellular-like medium containing (120 mM KCl, 10 mM NaCl, 1 mM KH2PO4, 20 mM HEPES-Tris, pH 7.2), 1.5 μM thapsigargin to inhibit SERCA so that the movement of Ca2+ was solely influenced by mitochondrial uptake, 20-μg/ml digitonin, supplemented with 2.5 μM succinate. All solutions underwent Chelex 100 treatment to eliminate traces of Ca^{2+} (Sigma). Digitonin-permeabilized cells were loaded with the ratiometric reporters FuraFF at a concentration of 1 μM. Fluorescence was recorded using spectrofluorometer (Delta RAM, Photon Technology Int.) at 340- and 380-nm ex/510-nm em. Following baseline recordings, a repetitive series of Ca^{2+} boluses (5 μM) were introduced at indicated time points. Upon reaching a steady state recording, a protonophore, 10 μM FCCP, was added to collapse the $\Delta\psi m$ and release matrix free-Ca^{2+}. The number of Ca^{2+} boluses taken up by cells was counted to calculate mitochondrial CRC.

Data Analysis

GraphPad Prism (La Jolla, CA, USA), was used for all statistical analysis. All experiments involving SBF-SEM and TEM data had at least three independent experiments. Statistics were not handled by those conducting the experiments. The black bars represent the standard error of the mean. For all analysis, one-way ANOVA was performed with tests against each independent group and significance was assessed using Fisher's protected least significant difference (LSD) test. *, **, ***, **** were set to show significant difference, denoting $p < 0.05$, $p < 0.01$, $p < 0.001$, and $p < 0.0001$, respectively.

FUNDING

All authors have no competing interests.

This project was funded by the National Institute of Health (NIH) NIDDK T-32, number DK007563 entitled Multidisciplinary Training in Molecular Endocrinology to Z.V.; National Institute of Health (NIH) NIDDK T-32, number DK007563 entitled Multidisciplinary Training

in Molecular Endocrinology to A.C.; NSF MCB #2011577I to S.A.M.; The UNCF/Bristol-Myers Squibb E.E. Just Faculty Fund, Career Award at the Scientific Interface (CASI Award) from Burroughs Welcome Fund (BWF) ID # 1021868.01, BWF Ad-hoc Award, NIH Small Research Pilot Subaward to 5R25HL106365-12 from the National Institutes of Health PRIDE Program, DK020593, Vanderbilt Diabetes and Research Training Center for DRTC Alzheimer's Disease Pilot & Feasibility Program. CZI Science Diversity Leadership grant number 2022- 253529 from the Chan Zuckerberg Initiative DAF, an advised fund of Silicon Valley Community Foundation to A.H.J.; and National Institutes of Health grant HD090061 and the Department of Veterans Affairs Office of Research Award I01 BX005352 to J.G. Howard Hughes Medical Institute Hanna H. Gray Fellows Program Faculty Phase (Grant# GT15655 awarded to M.R.M); and Burroughs Wellcome Fund PDEP Transition to Faculty (Grant# 1022604 awarded to M.R.M). National Institutes of Health Grants: R21DK119879 (to C.R.W.) and R01DK-133698 (to C.R.W.), American Heart Association Grant 16SDG27080009 (to C.R.W.) and by an American Society of Nephrology KidneyCure Transition to Independence Grant (to C.R.W.). Doris Duke Clinical Scientist Development Award grant 2021193, Burroughs Wellcome Fund grant 1021480, K23 HL156759, and R01 DK112262 (CNW). NIH Grants R01HL147818, R03HL155041, and R01HL144941 (A. Kirabo). NIH Grant R00DK120876 (D.T.), Harold S. Geneen Charitable Trust Awards Program (D.T.), Alzheimer's Association AARG-NTF-23-1144888 (D.T.). NIH Grant R00AG065445 (P.J.), Alzheimer's Association 24AARG-D-1191292 (P.J.), Wake ADRC REC and Development grant P30AG072947 (P.J.). American Heart Association Grant 23POST1020344 (A.K.). NIH K01AG062757 to (M.T.S.**)** Its contents are solely the responsibility of the authors and do not necessarily represent the official view of the NIH. The contents are solely the responsibility of the authors and do not necessarily represent the official view of the NIH. The funders had no role in study design, data collection, and analysis, decision to publish, or preparation of the manuscript. We would also like to acknowledge the Huck Institutes' Metabolomics Core Facility (RRID:SCR_023864) for use of the OE 240 LCMS and Drs. Imhoi Koo, Ashley Shay, and Sergei Koshkin for helpful discussions on sample preparation and analysis.

CONFLICT OF INTEREST

The authors declare that they have no conflict of interest.

References:

1. Ferguson, M. A. & Waikar, S. S. Established and Emerging Markers of Kidney Function. *Clinical Chemistry* **58**, 680–689 (2012).
2. Ishimoto, Y. & Inagi, R. Mitochondria: a therapeutic target in acute kidney injury. *Nephrology Dialysis Transplantation* **31**, 1062–1069 (2016).
3. Chronic Kidney Disease in the United States, 2019. *Fluoride Action Network* https://fluoridealert.org/studytracker/38332/ (2020).

4. Duann, P. & Lin, P.-H. Mitochondria Damage and Kidney Disease. in *Mitochondrial Dynamics in Cardiovascular Medicine* (ed. Santulli, G.) 529–551 (Springer International Publishing, Cham, 2017). doi:10.1007/978-3-319-55330-6_27.
5. Bhargava, P. & Schnellmann, R. G. Mitochondrial energetics in the kidney. *Nat Rev Nephrol* **13**, 629–646 (2017).
6. Glancy, B. Visualizing mitochondrial form and function within the cell. *Trends in molecular medicine* **26**, 58–70 (2020).
7. Picard, M. & McEwen, B. S. Mitochondria impact brain function and cognition. *Proceedings of the National Academy of Sciences* **111**, 7–8 (2014).
8. Duchen, M. R. & Szabadkai, G. Roles of mitochondria in human disease. *Essays in Biochemistry* **47**, 115–137 (2010).
9. Mao, J. *et al.* The relationship between kidney disease and mitochondria: a bibliometric study. *Renal Failure* **46**, 2302963 (2024).
10. Parasyri, M. *et al.* Renal Phenotype in Mitochondrial Diseases: A Multicenter Study. *Kidney Diseases* **8**, 148–159 (2022).
11. Forbes, J. M. & Thorburn, D. R. Mitochondrial dysfunction in diabetic kidney disease. *Nat Rev Nephrol* **14**, 291–312 (2018).
12. Alway, S. E., Mohamed, J. S. & Myers, M. J. Mitochondria Initiate and Regulate Sarcopenia. *Exerc Sport Sci Rev* **45**, 58–69 (2017).
13. Hepple, R. T. Mitochondrial Involvement and Impact in Aging Skeletal Muscle. *Frontiers in Aging Neuroscience* **6**, (2014).
14. Flannery, P. J. & Trushina, E. Mitochondrial dynamics and transport in Alzheimer's disease. *Molecular and Cellular Neuroscience* **98**, 109–120 (2019).

15. Zhang, L. *et al.* Altered brain energetics induces mitochondrial fission arrest in Alzheimer's Disease. *Scientific reports* **6**, 1–12 (2016).
16. Boudina, S. *et al*. Mitochondrial energetics in the heart in obesity-related diabetes: direct evidence for increased uncoupled respiration and activation of uncoupling proteins. *Diabetes* **56**, 2457–2466 (2007).
17. Friederich, M., Hansell, P. & Palm, F. Diabetes, oxidative stress, nitric oxide and mitochondria function. *Current diabetes reviews* **5**, 120–144 (2009).
18. Venkatachalam, M. A. & Weinberg, J. M. The tubule pathology of septic acute kidney injury: a neglected area of research comes of age. *Kidney International* **81**, 338–340 (2012).
19. Padovano, V., Podrini, C., Boletta, A. & Caplan, M. J. Metabolism and mitochondria in polycystic kidney disease research and therapy. *Nat Rev Nephrol* **14**, 678–687 (2018).
20. Fieni, F., Bae Lee, S., Jan, Y. N. & Kirichok, Y. Activity of the mitochondrial calcium uniporter varies greatly between tissues. *Nat Commun* **3**, 1317 (2012).
21. Bratic, A. & Larsson, N.-G. The role of mitochondria in aging. *The Journal of clinical investigation* **123**, 951–957 (2013).
22. Stenvinkel, P. & Larsson, T. E. Chronic Kidney Disease: A Clinical Model of Premature Aging. *American Journal of Kidney Diseases* **62**, 339–351 (2013).
23. Perico, N., Remuzzi, G. & Benigni, A. Aging and the kidney. *Current Opinion in Nephrology and Hypertension* **20**, 312–317 (2011).
24. Figueiredo, P. A., Mota, M. P., Appell, H. J. & Duarte, J. A. The role of mitochondria in aging of skeletal muscle. *Biogerontology* **9**, 67–84 (2008).
25. Lesnefsky, E. J., Chen, Q. & Hoppel, C. L. Mitochondrial Metabolism in Aging Heart. *Circ Res* **118**, 1593–1611 (2016).

26. Zhang, J. *et al.* Alterations in mitochondrial dynamics with age-related Sirtuin1/Sirtuin3 deficiency impair cardiomyocyte contractility. *Aging Cell* **20**, e13419 (2021).
27. Serviddio, G. *et al.* Bioenergetics in aging: mitochondrial proton leak in aging rat liver, kidney and heart. *Redox Report* **12**, 91–95 (2007).
28. Yamamoto, T. *et al.* Time-dependent dysregulation of autophagy: Implications in aging and mitochondrial homeostasis in the kidney proximal tubule. *Autophagy* **12**, 801–813 (2016).
29. Cui, J. *et al.* Age-related changes in the function of autophagy in rat kidneys. *AGE* **34**, 329–339 (2012).
30. Neikirk, K. *et al.* Call to Action to Properly Utilize Electron Microscopy to Measure Organelles to Monitor Disease. *European Journal of Cell Biology* 151365 (2023) doi:10.1016/j.ejcb.2023.151365.
31. Jenkins, B. C. *et al.* Mitochondria in disease: changes in shapes and dynamics. *Trends Biochem Sci* **49**, 346–360 (2024).
32. Marshall, A. G. *et al.* Serial Block Face-Scanning Electron Microscopy as a Burgeoning Technology. *Adv Biol (Weinh)* e2300139 (2023) doi:10.1002/adbi.202300139.
33. Courson, J. A. *et al.* Serial Block-Face Scanning Electron Microscopy (SBF-SEM) of Biological Tissue Samples. *J Vis Exp* 10.3791/62045 (2021) doi:10.3791/62045.
34. Dutta, S. & Sengupta, P. Men and mice: Relating their ages. *Life Sci* **152**, 244–248 (2016).
35. Li, M. S. *et al.* NADPH oxidase-2 mediates zinc deficiency-induced oxidative stress and kidney damage. *American Journal of Physiology-Cell Physiology* **312**, C47–C55 (2017).
36. Tomsa, A. M., Alexa, A. L., Junie, M. L., Rachisan, A. L. & Ciumarnean, L. Oxidative stress as a potential target in acute kidney injury. *PeerJ* **7**, e8046 (2019).

37. Genin, E. C. *et al.* CHCHD 10 mutations promote loss of mitochondrial cristae junctions with impaired mitochondrial genome maintenance and inhibition of apoptosis. *EMBO molecular medicine* **8**, 58–72 (2016).

38. Vue, Z. *et al.* Three-Dimensional Mitochondria Reconstructions of Murine Cardiac Muscle Changes in Size Across Aging. *American Journal of Physiology-Heart and Circulatory Physiology* (2023) doi:10.1152/ajpheart.00202.2023.

39. Vue, Z. *et al.* Mouse Skeletal Muscle Decrease in the MICOS Complex and Altered Mitochondrial Networks with age. *bioRxiv* 2022–03 (2022).

40. Gyurászová, M., Gurecká, R., Bábíčková, J. & Tóthová, Ľ. Oxidative Stress in the Pathophysiology of Kidney Disease: Implications for Noninvasive Monitoring and Identification of Biomarkers. *Oxid Med Cell Longev* **2020**, 5478708 (2020).

41. Hill Gallant, K. M. & Spiegel, D. M. Calcium Balance in Chronic Kidney Disease. *Curr Osteoporos Rep* **15**, 214–221 (2017).

42. Childs, D. D. *et al.* In-phase signal intensity loss in solid renal masses on dual-echo gradient-echo MRI: association with malignancy and pathologic classification. *AJR Am J Roentgenol* **203**, W421-428 (2014).

43. Outwater, E. K., Bhatia, M., Siegelman, E. S., Burke, M. A. & Mitchell, D. G. Lipid in renal clear cell carcinoma: detection on opposed-phase gradient-echo MR images. *Radiology* **205**, 103–107 (1997).

44. Fang, Y. *et al.* The ageing kidney: Molecular mechanisms and clinical implications. *Ageing Research Reviews* **63**, 101151 (2020).

45. Wang, K., Liao, Q. & Chen, X. Research progress on the mechanism of renal interstitial fibrosis in obstructive nephropathy. *Heliyon* **9**, e18723 (2023).

46. Menn-Josephy, H. *et al.* Renal interstitial fibrosis: an imperfect predictor of kidney disease progression in some patient cohorts. *Am J Nephrol* **44**, 289–299 (2016).

47. Chu, Y. *et al.* Glutathione peroxidase 1 overexpression reduces oxidative stress, and improves pathology and proteome remodeling in the kidneys of old mice. *Aging Cell* **19**, e13154 (2020).

48. Lv, W., Booz, G. W., Fan, F., Wang, Y. & Roman, R. J. Oxidative Stress and Renal Fibrosis: Recent Insights for the Development of Novel Therapeutic Strategies. *Front Physiol* **9**, 105 (2018).

49. Walker, L. M. *et al.* Oxidative Stress and Reactive Nitrogen Species Generation during Renal Ischemia. *Toxicological Sciences* **63**, 143–148 (2001).

50. Qian, J. *et al.* Nitrotyrosine Level Was Associated with Mortality in Patients with Acute Kidney Injury. *PLOS ONE* **8**, e79962 (2013).

51. Brandt, T. *et al.* Changes of mitochondrial ultrastructure and function during ageing in mice and Drosophila. *eLife* **6**, e24662.

52. L, G., Nn, van der W., Ij, O., Pj, P. & Am, van der B. Loss of the intermembrane space protein Mgm1/OPA1 induces swelling and localized constrictions along the lengths of mitochondria. *The Journal of biological chemistry* **279**, (2004).

53. Cogliati, S., Enriquez, J. A. & Scorrano, L. Mitochondrial cristae: where beauty meets functionality. *Trends in biochemical sciences* **41**, 261–273 (2016).

54. Eisner, V. *et al.* Mitochondrial fusion dynamics is robust in the heart and depends on calcium oscillations and contractile activity. *Proc Natl Acad Sci U S A* **114**, E859–E868 (2017).

55. Lam, J. *et al.* A Universal Approach to Analyzing Transmission Electron Microscopy with ImageJ. *Cells* **10**, 2177 (2021).

56. Crabtree, A. *et al.* Defining Mitochondrial Cristae Morphology Changes Induced by Aging in Brown Adipose Tissue. *Adv Biol (Weinh)* e2300186 (2023) doi:10.1002/adbi.202300186.

57. McBride, E. L. *et al.* Comparison of 3D cellular imaging techniques based on scanned electron probes: Serial block face SEM vs. Axial bright-field STEM tomography. *Journal of Structural Biology* **202**, 216–228 (2018).

58. Anand, R., Reichert, A. S. & Kondadi, A. K. Emerging Roles of the MICOS Complex in Cristae Dynamics and Biogenesis. *Biology (Basel)* **10**, 600 (2021).

59. Friedman, J. R., Mourier, A., Yamada, J., McCaffery, J. M. & Nunnari, J. MICOS coordinates with respiratory complexes and lipids to establish mitochondrial inner membrane architecture. *Elife* **4**, e07739 (2015).

60. Vue, Z. *et al.* 3D reconstruction of murine mitochondria reveals changes in structure during aging linked to the MICOS complex. *Aging Cell* **22**, e14009 (2023).

61. Feng, Y., Madungwe, N. B. & Bopassa, J. C. Mitochondrial inner membrane protein, Mic60/mitofilin in mammalian organ protection. *J Cell Physiol* **234**, 3383–3393 (2019).

62. An, J. *et al.* CHCM1/CHCHD6, Novel Mitochondrial Protein Linked to Regulation of Mitofilin and Mitochondrial Cristae Morphology *. *Journal of Biological Chemistry* **287**, 7411–7426 (2012).

63. Darshi, M. *et al.* ChChd3, an Inner Mitochondrial Membrane Protein, Is Essential for Maintaining Crista Integrity and Mitochondrial Function *. *Journal of Biological Chemistry* **286**, 2918–2932 (2011).

64. Darshi, M. & Taylor, S. S. Mitochondrial ChChD3 acts as a Scaffold for Mitofilin, Sam50 and PKA. (2008).

65. Barrera, M., Koob, S., Dikov, D., Vogel, F. & Reichert, A. S. OPA1 functionally interacts with MIC60 but is dispensable for crista junction formation. *FEBS Letters* **590**, 3309–3322 (2016).

66. Hu, C. *et al.* OPA1 and MICOS Regulate mitochondrial crista dynamics and formation. *Cell Death Dis* **11**, 1–17 (2020).

67. Gilkerson, R., De La Torre, P. & St. Vallier, S. Mitochondrial OMA1 and OPA1 as Gatekeepers of Organellar Structure/Function and Cellular Stress Response. *Frontiers in Cell and Developmental Biology* **9**, (2021).

68. Percy, C., Pat, B., Poronnik, P. & Gobe, G. Role of oxidative stress in age-associated chronic kidney pathologies. *Advances in Chronic Kidney Disease* **12**, 78–83 (2005).

69. Stenvinkel, P. *et al.* Chronic Inflammation in Chronic Kidney Disease Progression: Role of Nrf2. *Kidney Int Rep* **6**, 1775–1787 (2021).

70. Ding, C. *et al.* Mitofilin and CHCHD6 physically interact with Sam50 to sustain cristae structure. *Scientific reports* **5**, 1–11 (2015).

71. Tomar, D. *et al.* MICU1 regulates mitochondrial cristae structure and function independently of the mitochondrial Ca2+ uniporter channel. *Sci Signal* **16**, eabi8948 (2023).

72. Gottschalk, B. *et al.* MICU1 controls cristae junction and spatially anchors mitochondrial Ca2+ uniporter complex. *Nat Commun* **10**, 3732 (2019).

73. Hinton, A. *et al.* ATF4 Dependent Increase in Mitochondrial-Endoplasmic Reticulum Tethering Following OPA1 Deletion in Skeletal Muscle. *Journal of Cellular Physiology* (2024) doi:10.1101/2022.09.12.507669.

74. Csordás, G. & Hajnóczky, G. SR/ER–mitochondrial local communication: Calcium and ROS. *Biochimica et Biophysica Acta (BBA) - Bioenergetics* **1787**, 1352–1362 (2009).

75. Ilacqua, N., Anastasia, I. & Pellegrini, L. Isolation and analysis of fractions enriched in WrappER-associated mitochondria from mouse liver. *STAR Protocols* **2**, 100752 (2021).

76. Li, Q. & Hoppe, T. Role of amino acid metabolism in mitochondrial homeostasis. *Front Cell Dev Biol* **11**, 1127618 (2023).

77. Bárcena, C., Martínez, M. A., Ortega, M. P., Muñoz, H. G. & Sárraga, G. U. Mitochondria with Tubulovesicular Cristae in Renal Oncocytomas. *Ultrastructural Pathology* **34**, 315–320 (2010).

78. O'Toole, J. F., Patel, H. V., Naples, C. J., Fujioka, H. & Hoppel, C. L. Decreased cytochrome c mediates an age-related decline of oxidative phosphorylation in rat kidney mitochondria. *Biochemical Journal* **427**, 105–112 (2010).

79. Glancy, B., Kim, Y., Katti, P. & Willingham, T. B. The Functional Impact of Mitochondrial Structure Across Subcellular Scales. *Frontiers in Physiology* **11**, (2020).

80. Hara, Y. *et al.* Presynaptic mitochondrial morphology in monkey prefrontal cortex correlates with working memory and is improved with estrogen treatment. *Proceedings of the National Academy of Sciences* **111**, 486–491 (2014).

81. Zhou, Y. *et al.* Topology-dependent, bifurcated mitochondrial quality control under starvation. *Autophagy* **16**, 562–574 (2020).

82. Jankauskas, S. S. *et al.* Aged kidney: can we protect it? Autophagy, mitochondria and mechanisms of ischemic preconditioning. *Cell Cycle* **17**, 1291–1309 (2018).

83. Long, Q. *et al.* Modeling of Mitochondrial Donut Formation. *Biophysical journal* **109**, 892–9 (2015).

84. Balzer, M. S., Rohacs, T. & Susztak, K. How Many Cell Types Are in the Kidney and What Do They Do? *Annu Rev Physiol* **84**, 507–531 (2022).

85. Agarwal, S. K., Sethi, S. & Dinda, A. K. Basics of kidney biopsy: A nephrologist's perspective. *Indian J Nephrol* **23**, 243–252 (2013).

86. Samuel, C. S. Determination of Collagen Content, Concentration, and Sub-types in Kidney Tissue. in *Kidney Research: Experimental Protocols* (eds. Becker, G. J. & Hewitson, T. D.) 223–235 (Humana Press, Totowa, NJ, 2009). doi:10.1007/978-1-59745-352-3_16.

87. Jiang, M. *et al.* Mitochondrial dysfunction and the AKI-to-CKD transition. *American Journal of Physiology-Renal Physiology* **319**, F1105–F1116 (2020).

88. Bowes, T. & Gupta, R. S. Novel mitochondrial extensions provide evidence for a link between microtubule-directed movement and mitochondrial fission. *Biochemical and Biophysical Research Communications* **376**, 40–45 (2008).

89. Gomes, P. *et al.* Aging increases oxidative stress and renal expression of oxidant and antioxidant enzymes that are associated with an increased trend in systolic blood pressure. *Oxid Med Cell Longev* **2**, 138–145 (2009).

90. Zhou, X. J. *et al.* The aging kidney. *Kidney International* **74**, 710–720 (2008).

91. O'Sullivan, E. D., Hughes, J. & Ferenbach, D. A. Renal Aging: Causes and Consequences. *J Am Soc Nephrol* **28**, 407–420 (2017).

92. Rockfield, S. M. *et al.* Genetic ablation of Immt induces a lethal disruption of the MICOS complex. *Life Sci Alliance* **7**, e202302329 (2024).

93. Li, H. *et al.* Mic60/Mitofilin determines MICOS assembly essential for mitochondrial dynamics and mtDNA nucleoid organization. *Cell Death & Differentiation* **23**, 380–392 (2016).

94. Viana, M. P., Levytskyy, R. M., Anand, R., Reichert, A. S. & Khalimonchuk, O. Protease OMA1 modulates mitochondrial bioenergetics and ultrastructure through dynamic association with MICOS complex. *iScience* **24**, 102119 (2021).

95. Birker, K. *et al.* Mitochondrial MICOS complex genes, implicated in hypoplastic left heart syndrome, maintain cardiac contractility and actomyosin integrity. *eLife* **12**, e83385 (2023).

96. Dong, J. *et al.* Mic19 depletion impairs endoplasmic reticulum-mitochondrial contacts and mitochondrial lipid metabolism and triggers liver disease. *Nat Commun* **15**, 168 (2024).

97. Eramo, M. J., Lisnyak, V., Formosa, L. E. & Ryan, M. T. The 'mitochondrial contact site and cristae organising system' (MICOS) in health and human disease. *The Journal of Biochemistry* **167**, 243–255 (2020).

98. Warnsmann, V. *et al.* Disruption of the MICOS complex leads to an aberrant cristae structure and an unexpected, pronounced lifespan extension in Podospora anserina. *Journal of Cellular Biochemistry* **123**, 1306–1326 (2022).

99. Li, L. *et al.* A mitochondrial membrane-bridging machinery mediates signal transduction of intramitochondrial oxidation. *Nat Metab* **3**, 1242–1258 (2021).

100. Yang, Y. & Sauve, A. A. NAD+ metabolism: Bioenergetics, signaling and manipulation for therapy. *Biochim Biophys Acta* **1864**, 1787–1800 (2016).

101. Tomar, D. & Elrod, J. W. Metabolite regulation of the mitochondrial calcium uniporter channel. *Cell Calcium* **92**, 102288 (2020).

102. Zorov, D. B., Juhaszova, M. & Sollott, S. J. Mitochondrial Reactive Oxygen Species (ROS) and ROS-Induced ROS Release. *Physiol Rev* **94**, 909–950 (2014).

103. Batandier, C., Leverve, X. & Fontaine, E. Opening of the mitochondrial permeability transition pore induces reactive oxygen species production at the level of the respiratory chain complex I. *J Biol Chem* **279**, 17197–17204 (2004).

104. Vianello, A. *et al.* The mitochondrial permeability transition pore (PTP) — An example of multiple molecular exaptation? *Biochimica et Biophysica Acta (BBA) - Bioenergetics* **1817**, 2072–2086 (2012).

105. Xiong, Y. *et al.* Mitochondrial calcium uniporter promotes kidney aging in mice through inducing mitochondrial calcium-mediated renal tubular cell senescence. *Acta Pharmacol Sin* 1–14 (2024) doi:10.1038/s41401-024-01298-5.

106. Xu, L. *et al.* GLIS1 alleviates cell senescence and renal fibrosis through PGC1-α mediated mitochondrial quality control in kidney aging. *Free Radical Biology and Medicine* **209**, 171–184 (2023).

107. Li, G., Scull, C., Ozcan, L. & Tabas, I. NADPH oxidase links endoplasmic reticulum stress, oxidative stress, and PKR activation to induce apoptosis. *Journal of Cell Biology* **191**, 1113–1125 (2010).

108. Jeong, B. Y. *et al.* Oxidative stress caused by activation of NADPH oxidase 4 promotes contrast-induced acute kidney injury. *PLOS ONE* **13**, e0191034 (2018).

109. Ziegler, D. V., Martin, N. & Bernard, D. Cellular senescence links mitochondria-ER contacts and aging. *Commun Biol* **4**, 1–14 (2021).

110. Carreras-Sureda, A. *et al.* Non-canonical function of IRE1α determines mitochondria-associated endoplasmic reticulum composition to control calcium transfer and bioenergetics. *Nat Cell Biol* **21**, 755–767 (2019).

111. Anastasia, I. *et al.* Mitochondria-rough-ER contacts in the liver regulate systemic lipid homeostasis. *Cell Reports* **34**, 108873 (2021).

112. Ilacqua, N. *et al.* A three-organelle complex made by wrappER contacts with peroxisomes and mitochondria responds to liver lipid flux changes. *Journal of Cell Science* **135**, jcs259091 (2021).

113. Massudi, H. *et al.* Age-Associated Changes In Oxidative Stress and NAD+ Metabolism In Human Tissue. *PLOS ONE* **7**, e42357 (2012).

114. Bruzzone, S. *et al.* Extracellular NAD+ regulates intracellular calcium levels and induces activation of human granulocytes. *Biochem J* **393**, 697–704 (2006).

115. Yan, L.-J. NADH/NAD+ Redox Imbalance and Diabetic Kidney Disease. *Biomolecules* **11**, 730 (2021).

116. Lauritzen, K. H. *et al.* Impaired dynamics and function of mitochondria caused by mtDNA toxicity leads to heart failure. *American Journal of Physiology-Heart and Circulatory Physiology* **309**, H434–H449 (2015).

117. Khan, N. A. *et al.* mTORC1 regulates mitochondrial integrated stress response and mitochondrial myopathy progression. *Cell metabolism* **26**, 419–428 (2017).

118. Papadopoli, D. *et al.* mTOR as a central regulator of lifespan and aging. *F1000Res* **8**, F1000 Faculty Rev-998 (2019).

119. Ilter, D. *et al.* NADK-mediated *de novo* NADP(H) synthesis is a metabolic adaptation essential for breast cancer metastasis. *Redox Biology* **61**, 102627 (2023).

120. Bester, A. C. *et al.* Nucleotide Deficiency Promotes Genomic Instability in Early Stages of Cancer Development. *Cell* **145**, 435–446 (2011).

121. McReynolds, M. R. *et al*. NAD+ flux is maintained in aged mice despite lower tissue concentrations. *Cell Syst* **12**, 1160-1172.e4 (2021).

122. McReynolds, M. R., Chellappa, K. & Baur, J. A. Age-related NAD+ decline. *Exp Gerontol* **134**, 110888 (2020).

123. Mapuskar, K. A. *et al*. Mitochondrial Oxidative Metabolism: An Emerging Therapeutic Target to Improve CKD Outcomes. *Biomedicines* **11**, 1573 (2023).

124. Console, L. *et al.* The Link Between the Mitochondrial Fatty Acid Oxidation Derangement and Kidney Injury. *Front Physiol* **11**, 794 (2020).

125. Zheng Koh, D. H. & Saheki, Y. Regulation of Plasma Membrane Sterol Homeostasis by Nonvesicular Lipid Transport. *Contact (Thousand Oaks)* **4**, 25152564211042451 (2021).

126. Tian, S., Ohta, A., Horiuchi, H. & Fukuda, R. Oxysterol-binding protein homologs mediate sterol transport from the endoplasmic reticulum to mitochondria in yeast. *J Biol Chem* **293**, 5636–5648 (2018).

127. Tsuboi, K., Uyama, T., Okamoto, Y. & Ueda, N. Endocannabinoids and related N-acylethanolamines: biological activities and metabolism. *Inflamm Regen* **38**, 28 (2018).

128. Boachie, N. *et al.* Circulating Endocannabinoids and N-Acylethanolamines in Individuals with Cannabis Use Disorder-Preliminary Findings. *Brain Sci* **13**, 1375 (2023).

129. Peng, K.-Y. *et al.* Mitochondrial dysfunction-related lipid changes occur in nonalcoholic fatty liver disease progression. *J Lipid Res* **59**, 1977–1986 (2018).

130. Schenkel, L. C. & Bakovic, M. Formation and regulation of mitochondrial membranes. *Int J Cell Biol* **2014**, 709828 (2014).

131. Paradies, G., Paradies, V., Ruggiero, F. M. & Petrosillo, G. Role of Cardiolipin in Mitochondrial Function and Dynamics in Health and Disease: Molecular and Pharmacological Aspects. *Cells* **8**, 728 (2019).

132. Chen, W.-W., Chao, Y.-J., Chang, W.-H., Chan, J.-F. & Hsu, Y.-H. H. Phosphatidylglycerol Incorporates into Cardiolipin to Improve Mitochondrial Activity and Inhibits Inflammation. *Sci Rep* **8**, 4919 (2018).

133. Pereira, R. O. *et al.* OPA 1 deficiency promotes secretion of FGF 21 from muscle that prevents obesity and insulin resistance. *The EMBO journal* **36**, 2126–2145 (2017).

134. Garza-Lopez, E. *et al.* Protocols for Generating Surfaces and Measuring 3D Organelle Morphology Using Amira. *Cells* **11**, 65 (2022).

135. Neikirk, K. *et al.* Systematic Transmission Electron Microscopy-Based Identification and 3D Reconstruction of Cellular Degradation Machinery. *Advanced Biology* **7**, 2200221 (2023).

136. Hinton, A. *et al.* A Comprehensive Approach to Sample Preparation for Electron Microscopy and the Assessment of Mitochondrial Morphology in Tissue and Cultured Cells. *Adv Biol (Weinh)* e2200202 (2023) doi:10.1002/adbi.202200202.

137. Lu, W., Wang, L., Chen, L., Hui, S. & Rabinowitz, J. D. Extraction and Quantitation of Nicotinamide Adenine Dinucleotide Redox Cofactors. *Antioxidants & Redox Signaling* **28**, 167–179 (2018).

138. Wang, L. *et al.* Peak Annotation and Verification Engine for Untargeted LC–MS Metabolomics. *Anal. Chem.* **91**, 1838–1846 (2019).

139. Adusumilli, R. & Mallick, P. Data Conversion with ProteoWizard msConvert. in *Proteomics: Methods and Protocols* (eds. Comai, L., Katz, J. E. & Mallick, P.) 339–368 (Springer, New York, NY, 2017). doi:10.1007/978-1-4939-6747-6_23.

140. Hinton, A. *et al.* A comprehensive approach for artifact-free sample preparation and assessment of mitochondrial morphology in tissue and cultured cells. *bioRxiv* (2021).

Figure Legend:

<u>Main Figures:</u>

Graphical Abstract: Kidney aging causes a decline in the MICOS complex, concomitant with metabolic, lipidomic, and mitochondrial structural alterations.

Figure 1: Comparative analyses of kidney characteristics in young and old subjects differentiated by sex.
Cross-sectional imaging of kidney anatomy data from (A) females under 50 years old (aged 14–42 years old; n = 8), (B) males under 50 years old (aged 14–48 years old; n = 6), (C) females over 60 years old (aged 65–90 years old; n = 9), and (D) males over 60 years old (aged 60–88 years old; n = 11). (E) Measurements of left kidney cross-sectional area, calculated as the product of length and width, in females and (F) males. (G) Measurements of left kidney in-phase, representing when magnetic fields of fat and water molecules are in alignment, in females and (H) males. (I) Measurements of left kidney out-of-phase, representing when magnetic fields of fat and water molecules are not in alignment, in females and (J) males. (K) The ratio of the in-phase measurements to out-of-phase, in females and (L) males. For all panels, error bars indicate SEM, Mann–Whitney tests were used for statistical analysis, and statistical significance is denoted as ns (not significant), *$p < 0.05$, and **$p < 0.01$.

Figure 2: Changes in fibrosis and oxidative damage in kidney of young and old murine samples.
(A) Representative images of Masson trichrome staining of the kidney cortex in young (4–5 months old) and (B) old (21–23 months old) samples. (C) Quantification of blue areas. (D) Immunohistochemistry for nitrotyrosine (brown color) in young (4–5 months old) and (E) old (21–23 months old) samples. (F) Quantification of the staining density of nitrotyrosine. For all panels, dots represent independent samples, error bars indicate SEM, unpaired t-tests were used for statistical analysis, and statistical significance is denoted as ns (not significant), *$p < 0.05$, and **$p < 0.01$.

Figure 3: Changes in kidney tissue mitochondria and cristae across aging revealed in transmission electron microscopy (TEM). (A) Representative transmission electron micrographs for kidney tissue at 3 month and (B) two-year in male mice. Boxes show cristae magnified to enhance the details of cristae. (C) Quantification of key mitochondrial characteristics included mitochondrial area and (D) circularity index, which measures mitochondrial shape. (E) Total mitochondria in regions of interest quantification. (F) For cristae, cristae score (D), a measurement of the quality observed cristae, is shown. (G) Using serial block face scanning electron microscopy, representative images of cristae morphology in three-dimensions are shown in three-month and (H) 2-year samples. Each dot represents one mitochondrion, with a variable number in each condition with mitochondria measurements in 3 months having n of approximately 1050 and in 2 years of having n of approximately 1450. Cristae score has n of 1093. For all panels, error bars indicate SEM, mann–Whitney tests were used for statistical analysis, and significance values indicate ****$P \leq 0.0001$ and ns, not significant.

Figure 4: Schematic of reconstructing kidney tissue mitochondria using serial block facing-scanning electron microscopy (SBF-SEM). (A) Schematic depicting removal of the kidney. (B) Following embedded fixation, SBF-SEM allows for ortho-slice alignment. (C) Manual segmentation of ortho slices was performed to ultimately yield (D) 3-dimensional (3-D) reconstructions of mitochondria (E) 3-D reconstruction of individually colored mitochondria from a transverse view and longitudinal view in kidney tissue of different ages.

Figure 5: Changes in kidney tissue mitochondria morphology across aging revealed in serial block facing-scanning electron microscopy (SBF-SEM). (A) Representative SBF-SEM orthogonal (ortho) slice for kidney tissue in three-month and (A') 2-year samples. (B) 3-D reconstructions of mitochondria in male kidney tissues of three-months and 2-years (B') overlaid on ortho slices. (C) 3-D reconstructed and isolated mitochondria for clear visualization from three-months and (C') 2-years. (D) 3-D reconstructions were then quantified by 3-D area of the average mitochondria (E) perimeter of the average mitochondria, and (F), mitochondrial volume in kidney tissue from 3-month and 2-year samples. (D'-F') Individual values of the mitochondrion in each mouse to show intra-animal heterogeneity. (G) Mito-otyping to arrange mitochondria on the basis of their volume to view qualitative differences in morphology. Each dot represents the average of a single mouse with a varied number of mitochondria surveyed within each mouse (n=4, with each sample having 83-251 mitochondria). In total, 3-month samples included 740 mitochondria, while 2-year samples included 962 mitochondria, which were used for statistical analysis. For all panels, error bars indicate SEM, mann–Whitney tests were used for statistical analysis, and significance values indicate **$P \leq 0.01$, ***$P \leq 0.001$, and ns, not significant.

Figure 6: Transcription and Western Blotting of *Opa1* and mitochondrial contact site and cristae organizing system (MICOS) genes in aging kidney tissue. (A–D) Quantitative polymerase chain reaction (qPCR) analyzing the gene transcript fold changes of Opa-1 and MICOS across aging: (A) *Opa1* transcripts, (B) *Mitofilin* transcripts, (C) *Chchd3* transcript, and (D) *Chchd6* transcripts. (E) Western Blot of OPA1, mitochondrial dynamic proteins, and MICOS protein expression. For all panels, error bars indicate SEM, and Mann–Whitney tests were used for statistical analysis. Each dot represents an individual qPCR run (n=4). Significance values indicate ***$P \leq 0.001$ and ****$P \leq 0.0001$. For all western blotting experiments, n = 4.

Figure 7: Loss of mitochondrial contact site and cristae organizing system (MICOS) genes result in mitochondrial structure changes and oxidative stress in the kidney. **(A-E)** Individual knockout (KO) of *Opa1*, *Mitofilin*, *Chchd3*, and *Chchd6* and representative transmission electron micrographs. (F–H) quantification upon KO state of each MICOS gene and Opa1 (n = 10 cells) was performed in 3-D reconstruction: (F) average single mitochondrion area, (G) average single mitochondrion perimeter, (H) average single mitochondrion circularity index, and (I) average single mitochondrion length across individual MICOS KO. (J) 4′,6-diamidino-2-phenylindole (DAPI) staining, MitoPY1 (5 uM, 45 min at 370 c magnification of 60x), and merge channels in scramble-siRNA (control), MIC60-siRNA (*MITOFILIN* KD), and CHCHD6-siRNA (*CHCHD6* KD) transfected permeabilized HEK293 cells. (K) 4′,6-diamidino-2-phenylindole (DAPI) staining, MitoBright Deep Red (10 uM, 30 min at 37^0 c), DCFDA (10 uM, 30 min at 37^0 c, magnification of 60x), and merge channels in scramble-siRNA (control),

MIC60-siRNA (*MITOFILIN* KD), and CHCHD6-siRNA (*CHCHD6* KD) transfected permeabilized HEK293 cells. (L) Plate reader-based reactive oxygen species (ROS) quantification. (M) Microscopy-based ROS quantification of MitoPY1 orange, (N) DCFDA, and (O) MitoSox Deep Red. For all statistical tests, a one-way ANOVA statistical test was performed with Dunnett's multiple comparisons test. For 3D microscopy, each dot represents a mitochondrion, with their number varied between control (n=81), *Opa1* KO (n=153), *Chchd3* KO (n=139), *Chchd6* KO (n=180), and *Mitofilin* KO (n=156). Significance values indicate *P ≤ 0.05, **P ≤ 0.01, ***P ≤ 0.001 and ****P ≤ 0.0001; ns, not significant.

Figure 8: mCa^{2+} uptake and calcium retention capacity are reduced in *MITOFILIN* (MIC60) and *CHCHD6* knockdown HEK293 cells. (A) Representative traces of mitochondrial calcium uptake in scramble-siRNA (control), MIC60-siRNA (*MITOFILIN* KD), and CHCHD6-siRNA (*CHCHD6* KD) transfected permeabilized HEK293 cells. (B) Percentage of mCa2+ uptake rate calculated from (C) representative traces of mitochondrial calcium retention capacity in control, *MITOFILIN* KD, and *CHCHD6* KD HEK293 cells. The number of boluses of calcium taken up by cells is shown in circles. (D) Percentage change in mitochondrial calcium retention capacity calculated from representative traces of mitochondrial calcium retention capacity. (E) Western blot showing siRNA-mediated KD of *CHCHD6*/CHCHD6 in HEK293 cells. (F) Western blot showing siRNA-mediated KD of *MITOFILIN*/MIC60 in HEK293 cells. (G) Serial block face scanning electron microscopy obtained representative images of mitochondria endoplasmic reticulum contact site morphology overlaid on orthoslice and (H) isolated in three dimensions in three-month and (I-J) 2-year samples. For all statistical tests, one-way ANOVA statistical test was performed with Dunnett's multiple comparisons test. N=3-5 for all calcium experiments, as run in triplicates. Significance values indicate **P ≤ 0.01.

Figure 9. Global metabolomic profiling uncovers dysregulated metabolic pathways and lipid classes with age in kidney tissues. (A) Metabolomics heatmap showing the relative abundance of the top 25 metabolite hits with age. (B) Metabolic pathway analysis revealing cluster of metabolites related to signaling networks that are disrupted in the aging kidney. (D-M) Metabolite pools illustrating the metabolic pathways that are altered with age in the kidney– Redox/NAD^+ Metabolism and Amino Acid Metabolism/Biosynthesis. For each tissue and metabolite in the heatmaps, the aged samples were normalized to the median of the young samples and then log2 transformed. Young, n= 6; aged, n= 6. For all panels, error bars indicate SEM, ** indicates P≤ 0.01; and *P≤ 0.05, calculated with Student's t-test.

Figure 10: Global lipidomic profiling uncovers dysregulated metabolic pathways and lipid classes with age in kidney tissues. (A) Heatmap showing disrupted and enriched lipid classes based on comparisons between young and old kidney tissues. (B) Lipid class enrichment (C) and lipid chain length enrichment based on comparisons between young and old kidney. Significantly different lipid classes represented in the figures are those with adjusted p-values < 0.05 (note: p-values were adjusted to correct for multiple comparisons using an FDR procedure) and log fold changes greater than 1 or less than −1. Young, n= 6; aged, n= 6. For all panels, error bars indicate SEM, ** indicates P≤ 0.01; and *P≤ 0.05, calculated with Student's t-test.

<u>Supplement:</u>

Supplementary Figure 1: Comparative analyses of kidney characteristics in young and old participants. (A) Metrics defined in Figure 1 grouped to look at overall age-related differences, regardless of sex. (B) Kidney cross-sectional area (CSA), (C) in-phase measurement, (D) out-of-phase measurement, and (E) in-phase to out-of-phase ratio, differentiated by sex. One-way ANOVA statistical test performed with post hoc Tukey's test. Each dot represents an individual participant (n=6-11); full patient information is available in File 1. For all panels, error bars indicate SEM, significance values indicate $*P \leq 0.05$, $**P \leq 0.01$, $***P \leq 0.001$, and $****P \leq 0.0001$; ns, not significant.

Supplementary Figure 2: Global metabolomic and lipidomic profiling uncovers dysregulated metabolic pathways and lipid classes and chain lengths with age in kidney tissues. (SA) Metabolomics heatmap showing the relative abundance of metabolites.

Supplementary File 1: Full kidney characteristics, including age, of young and old participants analyzed in Figure 1.

Video 1: 3D reconstruction of mitochondria from various angles in 3-month kidney samples.

Video 2: 3D reconstruction of mitochondria from various angles in 2-year kidney samples.

Video 3: 3D reconstruction of wrappER (ER represented in green) from 3-month kidney samples.

Video 4: 3D reconstruction of MERCs (ER represented in blue) from 2-year kidney samples.

Graphical Abstract:

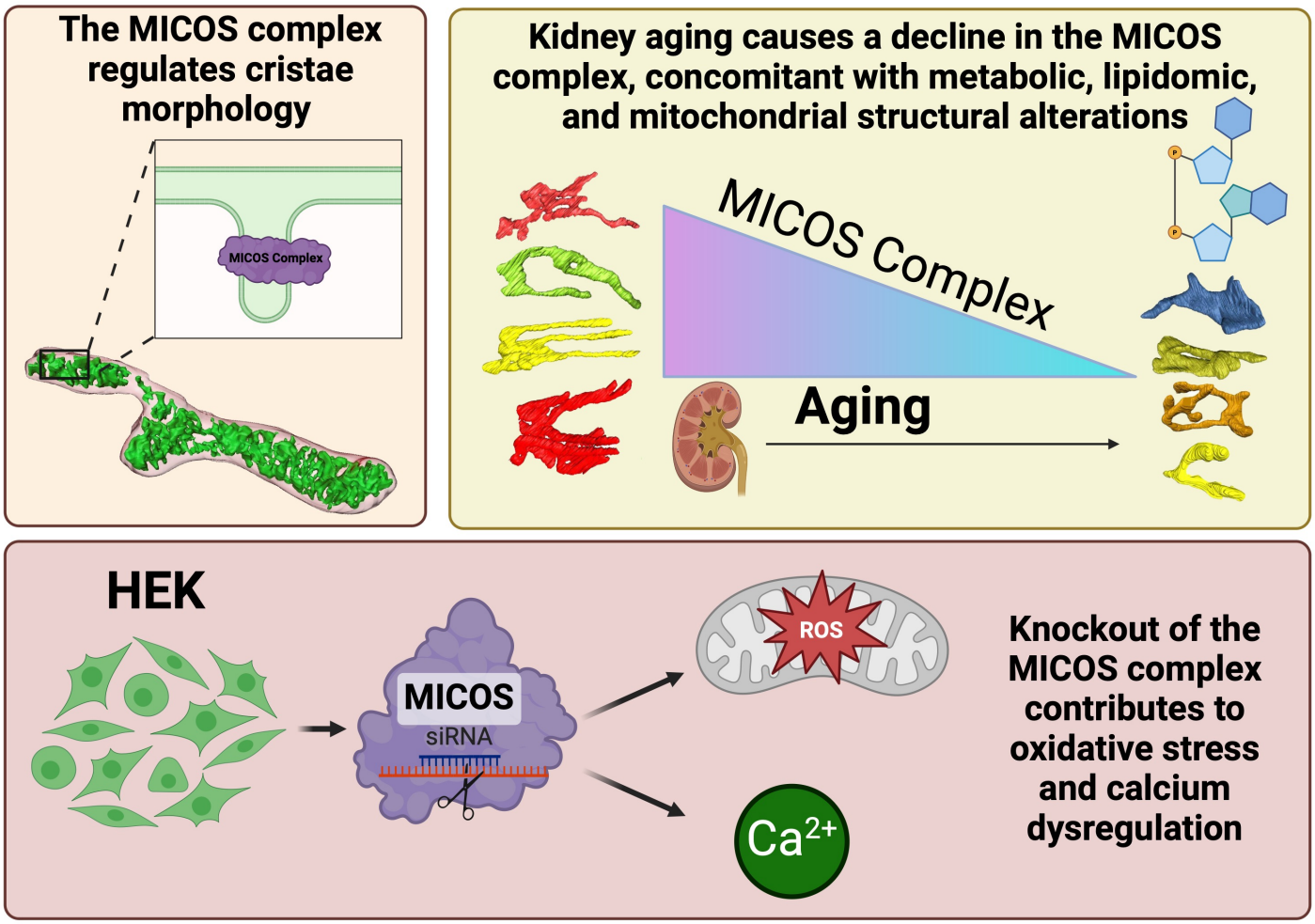

Figure 1

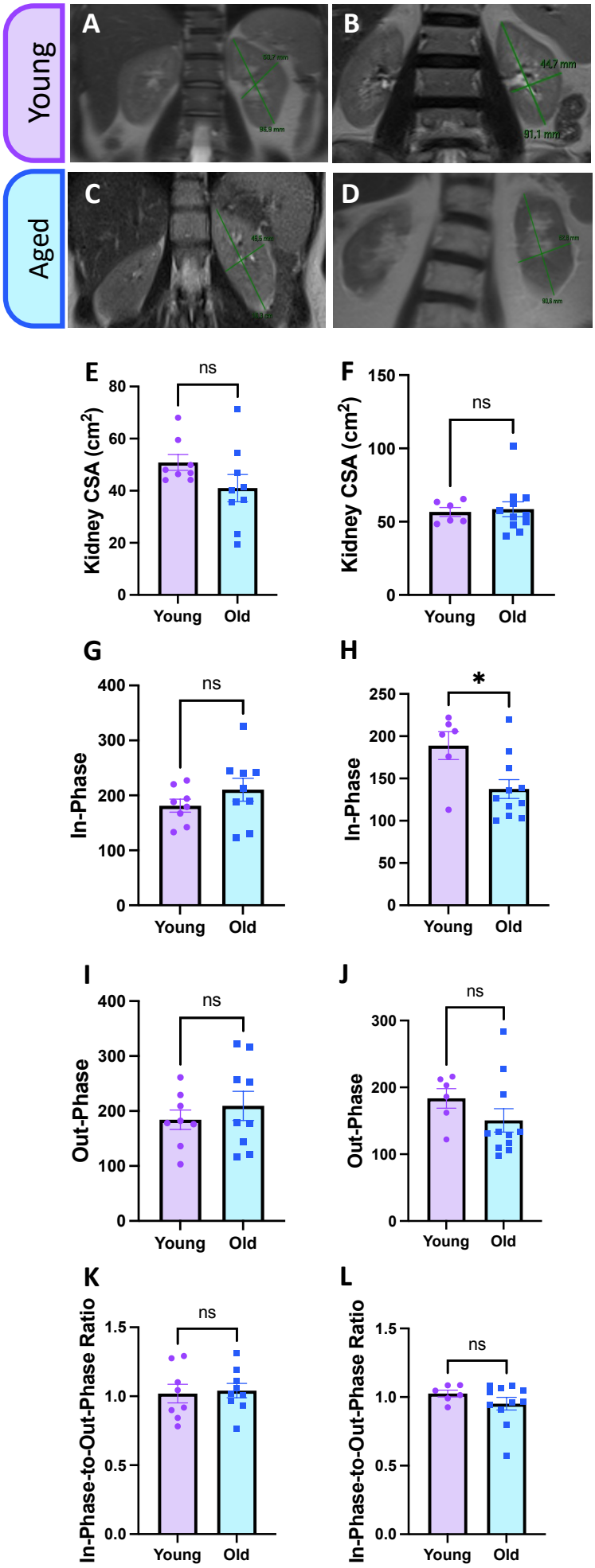
Female
Male
Young
Aged
A
B
C
D
44,7 mm
91,1 mm
E
F
G
H
I
J
K
L
Kidney CSA (cm²)
In-Phase
Out-Phase
In-Phase-to-Out-Phase Ratio
ns
*
Young
Old

Figure 2

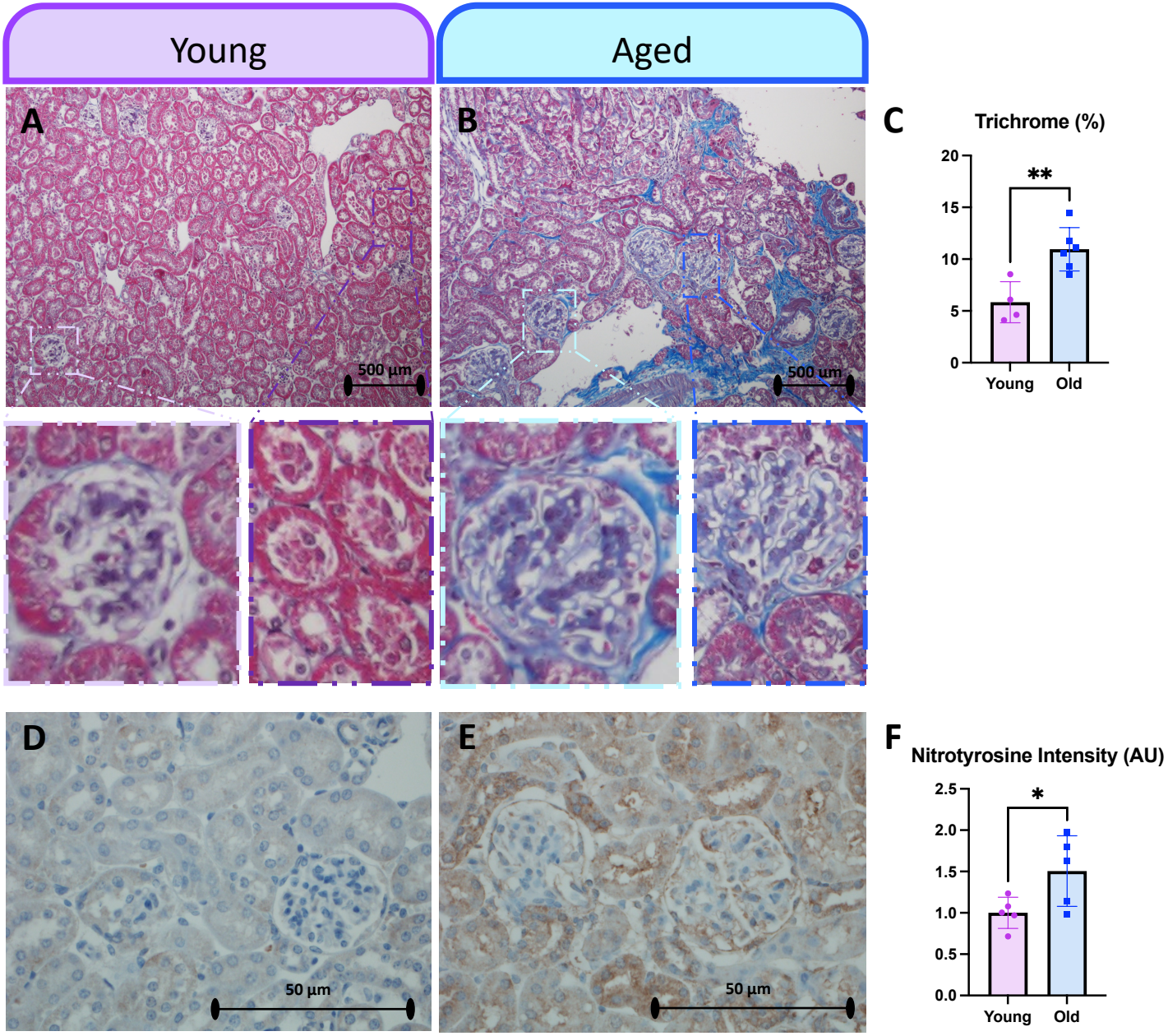
Young
Aged
A
B
500 µm
500 µm
C
Trichrome (%)
20
15
10
5
0
**
Young
Old
D
E
50 µm
50 µm
F
Nitrotyrosine Intensity (AU)
2.5
2.0
1.5
1.0
0.5
0.0
*
Young
Old

Figure 3

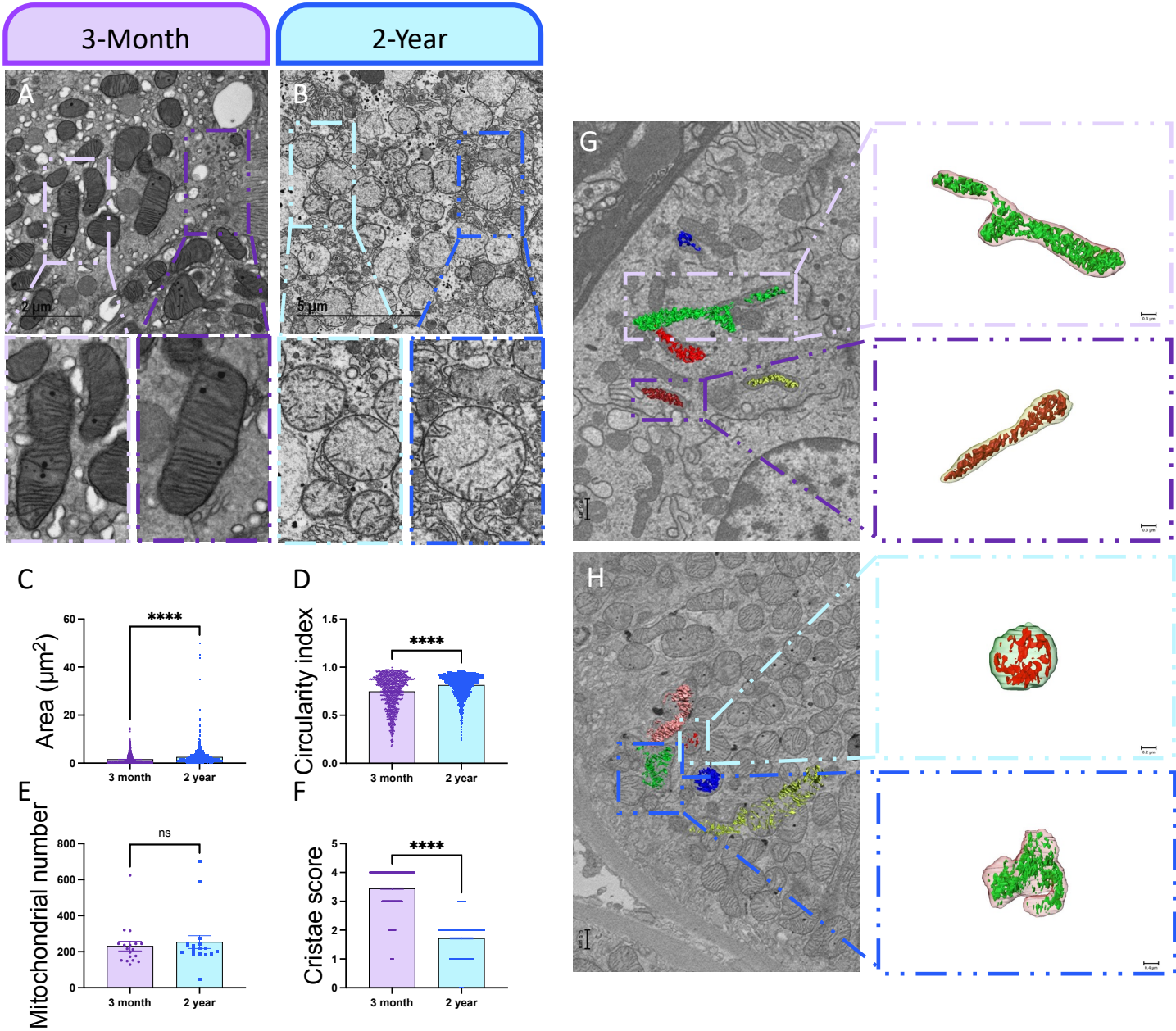
3-Month
2-Year
A
B
2 µm
5 µm
C
Area (µm²)
****
3 month
2 year
D
Circularity index
****
3 month
2 year
E
Mitochondrial number
ns
3 month
2 year
F
Cristae score
****
3 month
2 year
G
H

Figure 4

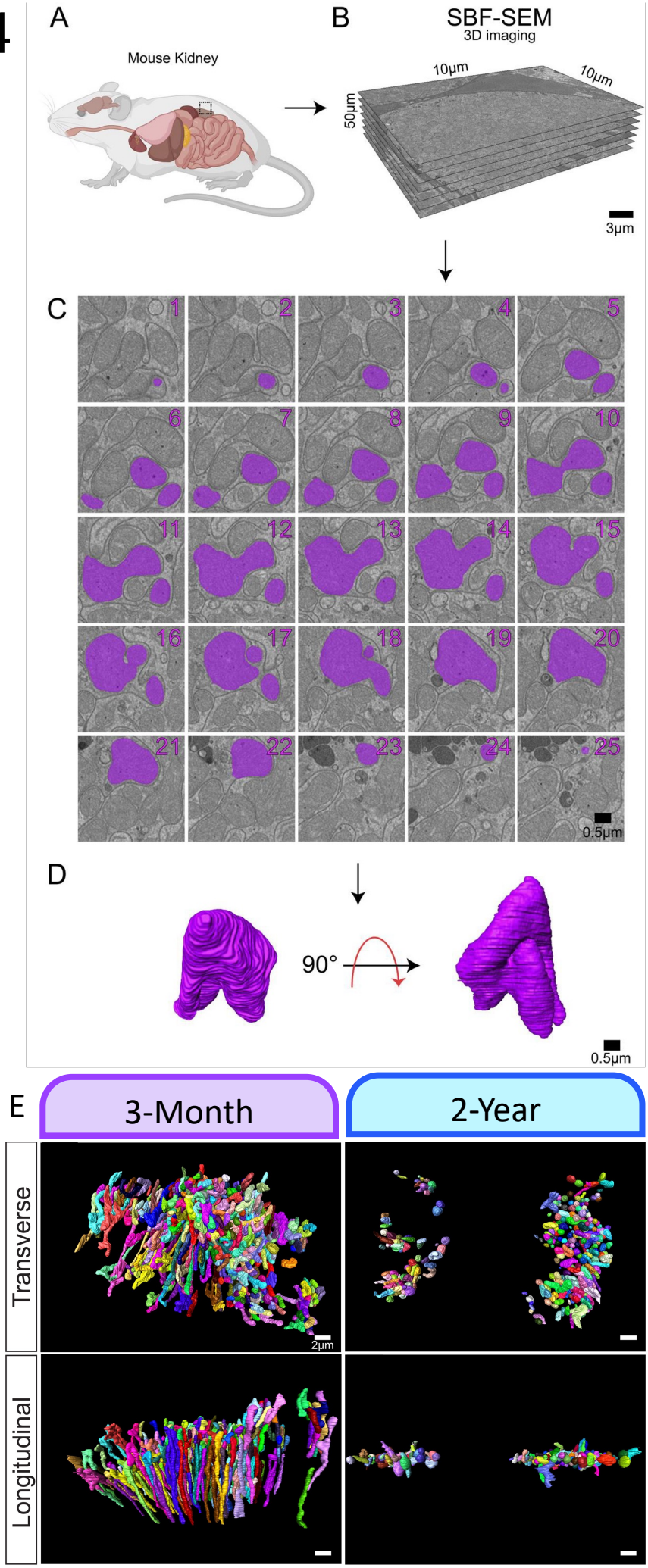
A
Mouse Kidney
B
SBF-SEM
3D imaging
10µm
10µm
50µm
3µm
C
1
2
3
4
5
6
7
8
9
10
11
12
13
14
15
16
17
18
19
20
21
22
23
24
25
0.5µm
D
90°
0.5µm
E
3-Month
2-Year
Transverse
Longitudinal
2µm

Figure 5

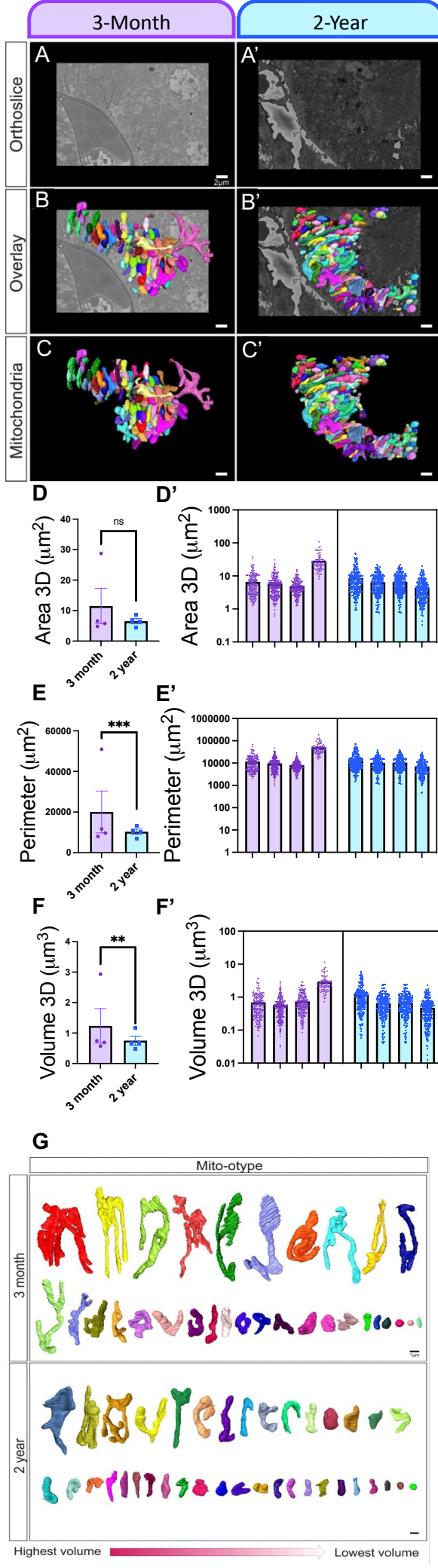
3-Month
2-Year
Orthoslice
Overlay
Mitochondria
A
A'
B
B'
C
C'
2µm
D
D'
Area 3D (µm2)
ns
3 month
2 year
E
E'
Perimeter (µm2)
***
F
F'
Volume 3D (µm3)
**
G
Mito-otype
3 month
2 year
Highest volume
Lowest volume

Figure 6

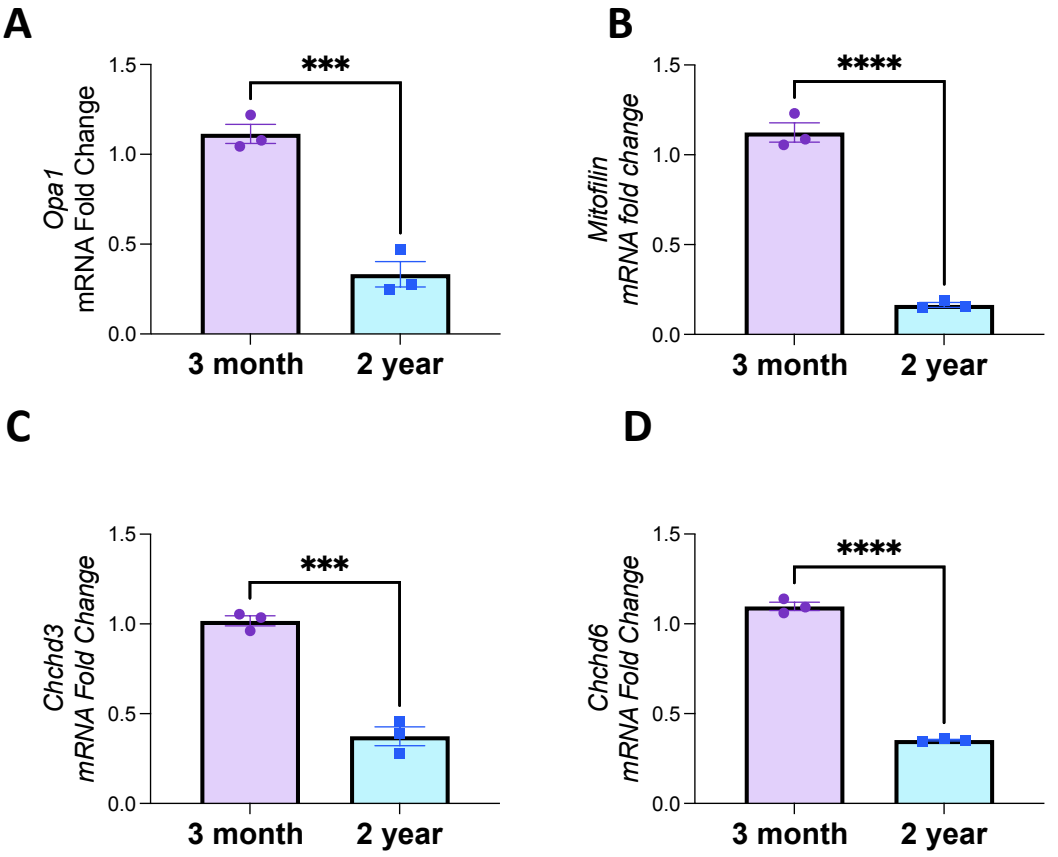
A
Opa1
mRNA Fold Change
1.5
1.0
0.5
0.0
***
3 month
2 year
B
Mitofilin
mRNA fold change
1.5
1.0
0.5
0.0
****
3 month
2 year
C
Chchd3
mRNA Fold Change
1.5
1.0
0.5
0.0
***
3 month
2 year
D
Chchd6
mRNA Fold Change
1.5
1.0
0.5
0.0
****
3 month
2 year

Figure 7

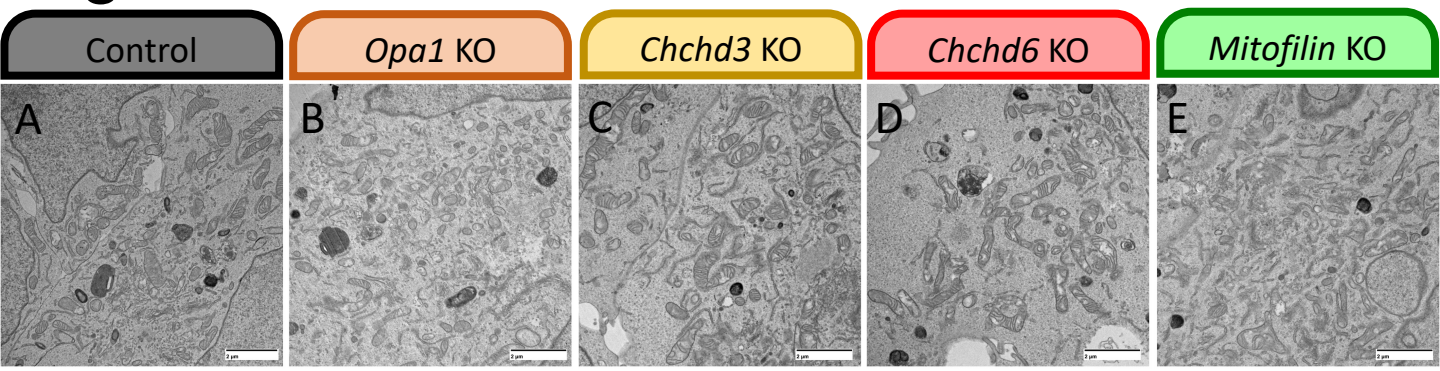
Control
Opa1 KO
Chchd3 KO
Chchd6 KO
Mitofilin KO
A
B
C
D
E

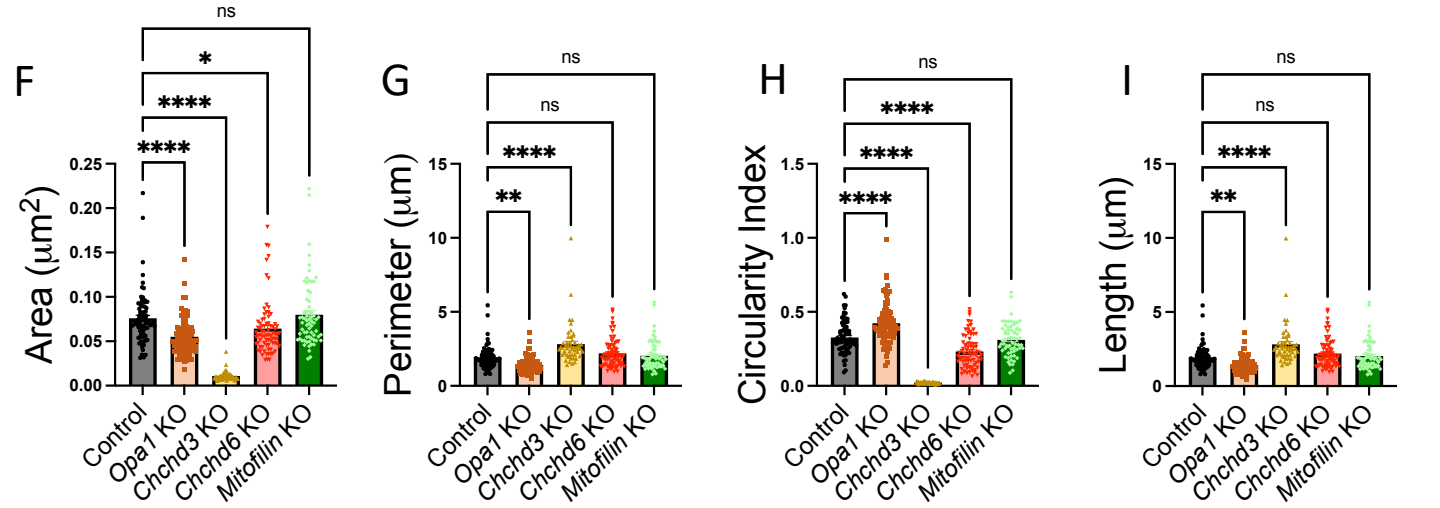
F
Area (µm²)
0.25
0.20
0.15
0.10
0.05
0.00
ns
*
****
****
G
Perimeter (µm)
15
10
5
0
ns
ns
****
**
H
Circularity Index
1.5
1.0
0.5
0.0
ns
****
****
****
I
Length (µm)
15
10
5
0
ns
ns
****
**
Control
Opa1 KO
Chchd3 KO
Chchd6 KO
Mitofilin KO

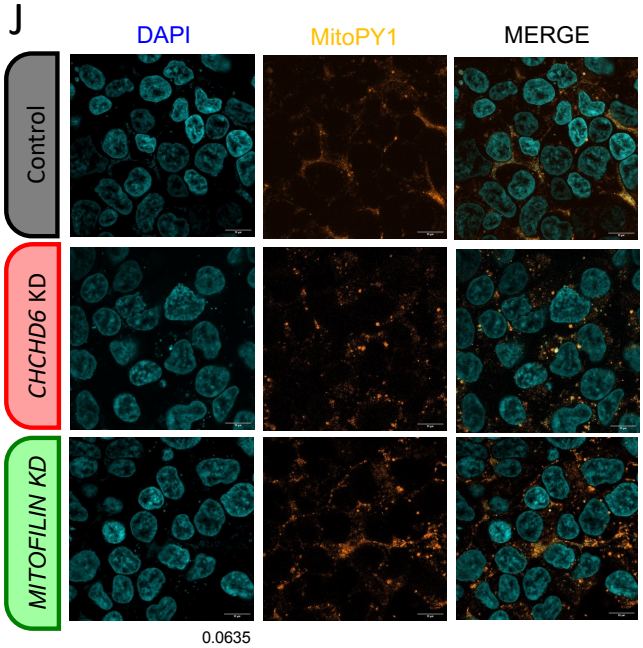
J
DAPI
MitoPY1
MERGE
Control
CHCHD6 KD
MITOFILIN KD

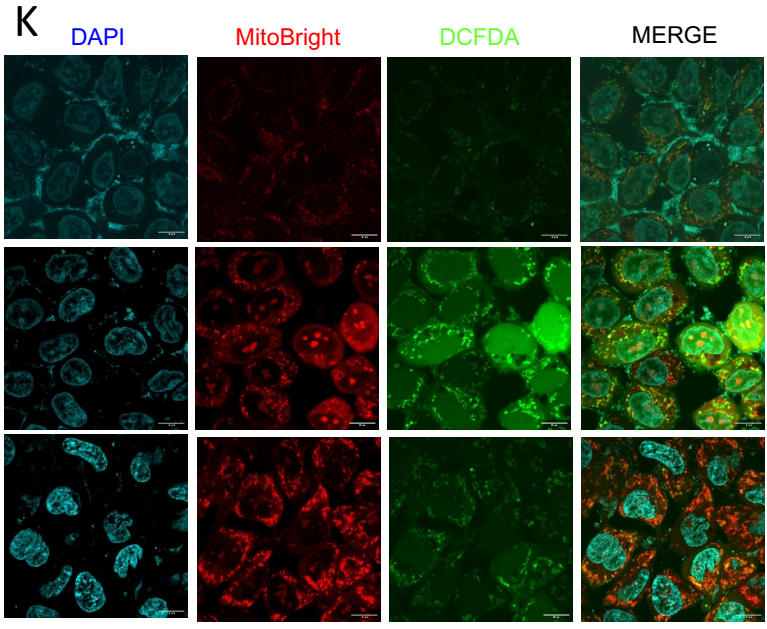
K
DAPI
MitoBright
DCFDA
MERGE

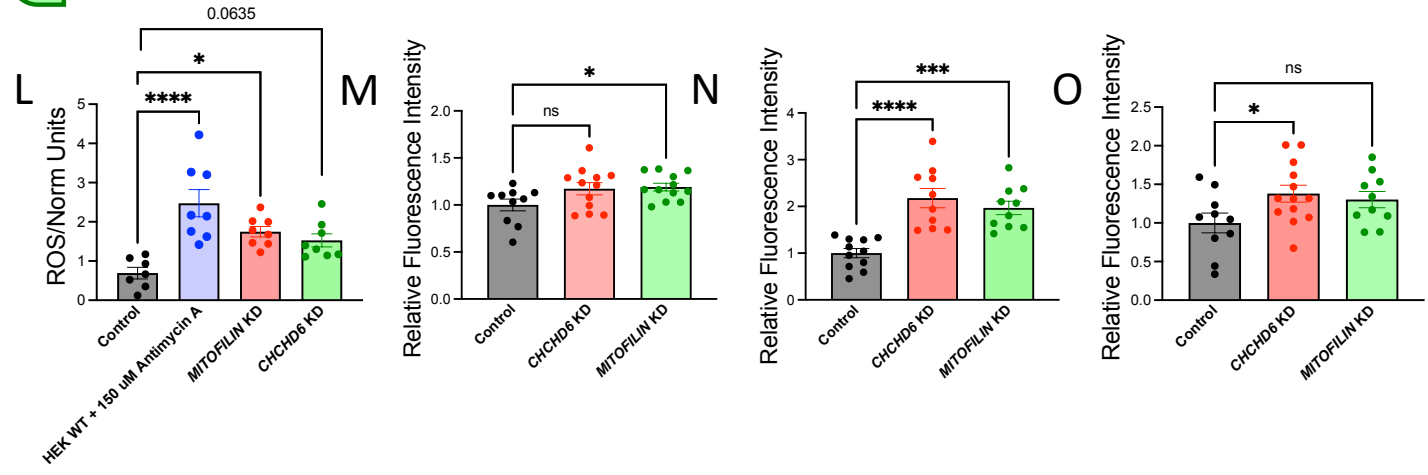
L
ROS/Norm Units
5
4
3
2
1
0
0.0635
*
****
Control
HEK WT + 150 uM Antimycin A
MITOFILIN KD
CHCHD6 KD
M
Relative Fluorescence Intensity
2.0
1.5
1.0
0.5
0.0
*
ns
N
Relative Fluorescence Intensity
4
3
2
1
0
***
****
O
Relative Fluorescence Intensity
2.5
2.0
1.5
1.0
0.5
0.0
ns
*
Control
CHCHD6 KD
MITOFILIN KD

Figure 8

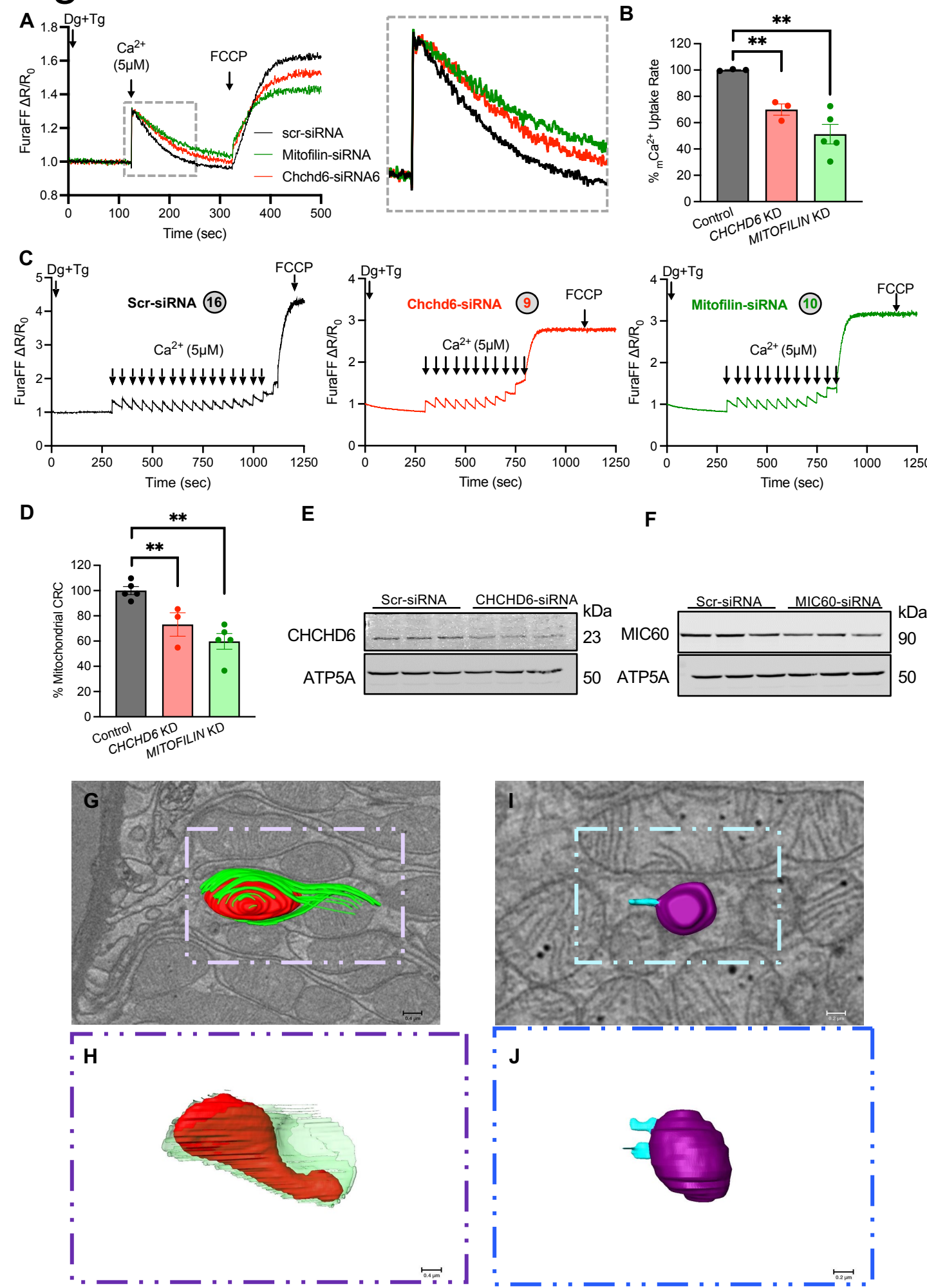
A
Dg+Tg
Ca2+ (5μM)
FCCP
FuraFF ΔR/R0
scr-siRNA
Mitofilin-siRNA
Chchd6-siRNA6
Time (sec)
B
% mCa2+ Uptake Rate
Control
CHCHD6 KD
MITOFILIN KD
C
Scr-siRNA 16
Chchd6-siRNA 9
Mitofilin-siRNA 10
D
% Mitochondrial CRC
E
Scr-siRNA
CHCHD6-siRNA
kDa
CHCHD6
23
ATP5A
50
F
Scr-siRNA
MIC60-siRNA
MIC60
90
G
H
I
J

Figure 9

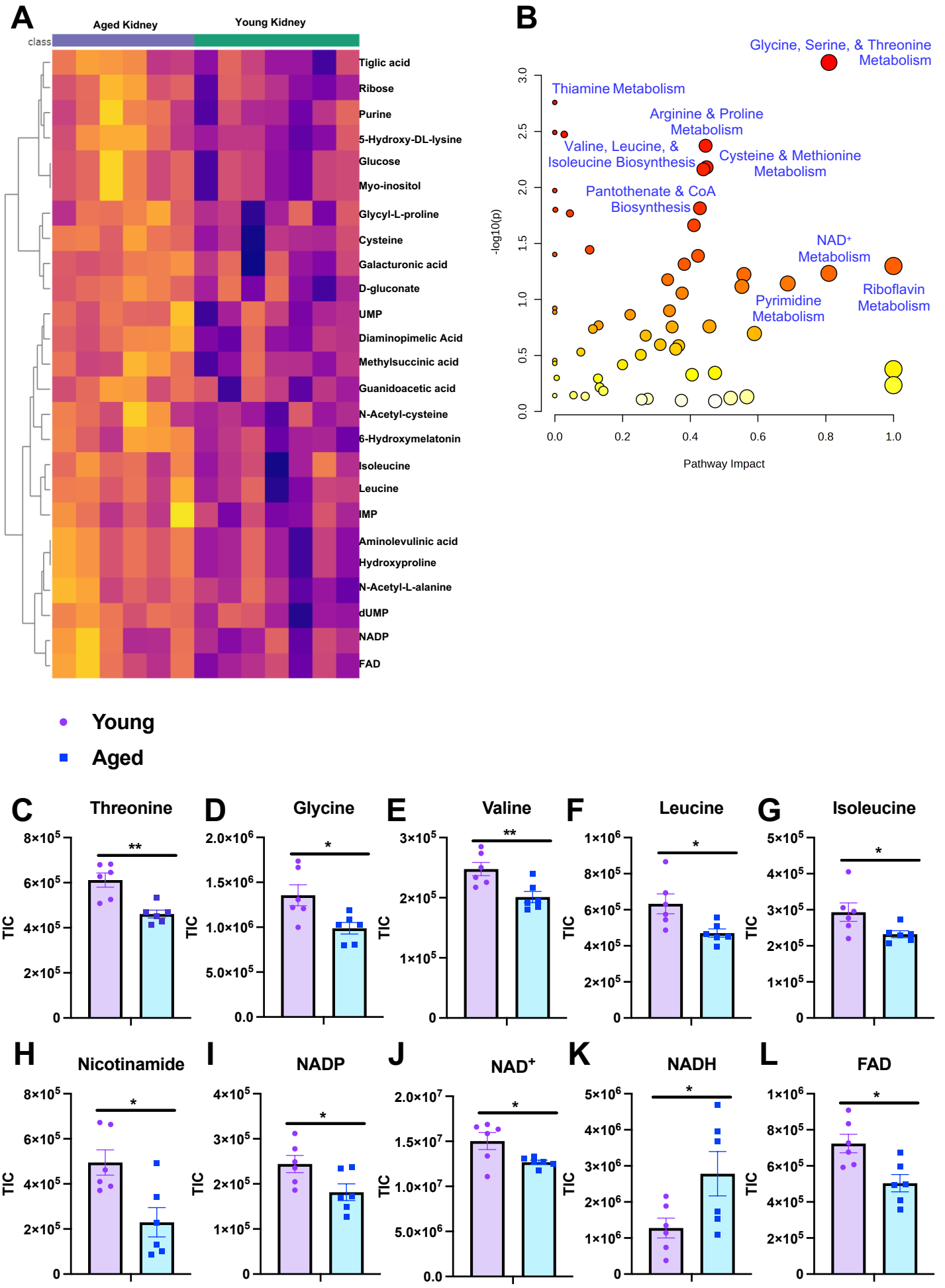
A
Aged Kidney
Young Kidney
class
Tiglic acid
Ribose
Purine
5-Hydroxy-DL-lysine
Glucose
Myo-inositol
Glycyl-L-proline
Cysteine
Galacturonic acid
D-gluconate
UMP
Diaminopimelic Acid
Methylsuccinic acid
Guanidoacetic acid
N-Acetyl-cysteine
6-Hydroxymelatonin
Isoleucine
Leucine
IMP
Aminolevulinic acid
Hydroxyproline
N-Acetyl-L-alanine
dUMP
NADP
FAD
B
Glycine, Serine, & Threonine Metabolism
Thiamine Metabolism
Arginine & Proline Metabolism
Valine, Leucine, & Isoleucine Biosynthesis
Cysteine & Methionine Metabolism
Pantothenate & CoA Biosynthesis
NAD+ Metabolism
Riboflavin Metabolism
Pyrimidine Metabolism
-log10(p)
Pathway Impact
Young
Aged
C Threonine
D Glycine
E Valine
F Leucine
G Isoleucine
H Nicotinamide
I NADP
J NAD+
K NADH
L FAD
TIC

Figure 10

A

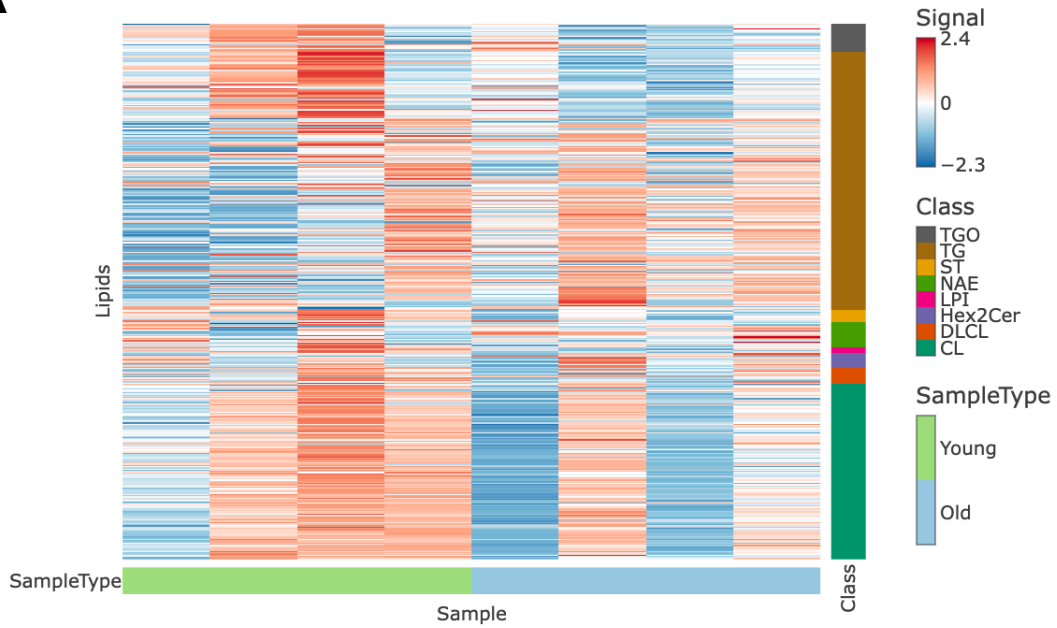

B

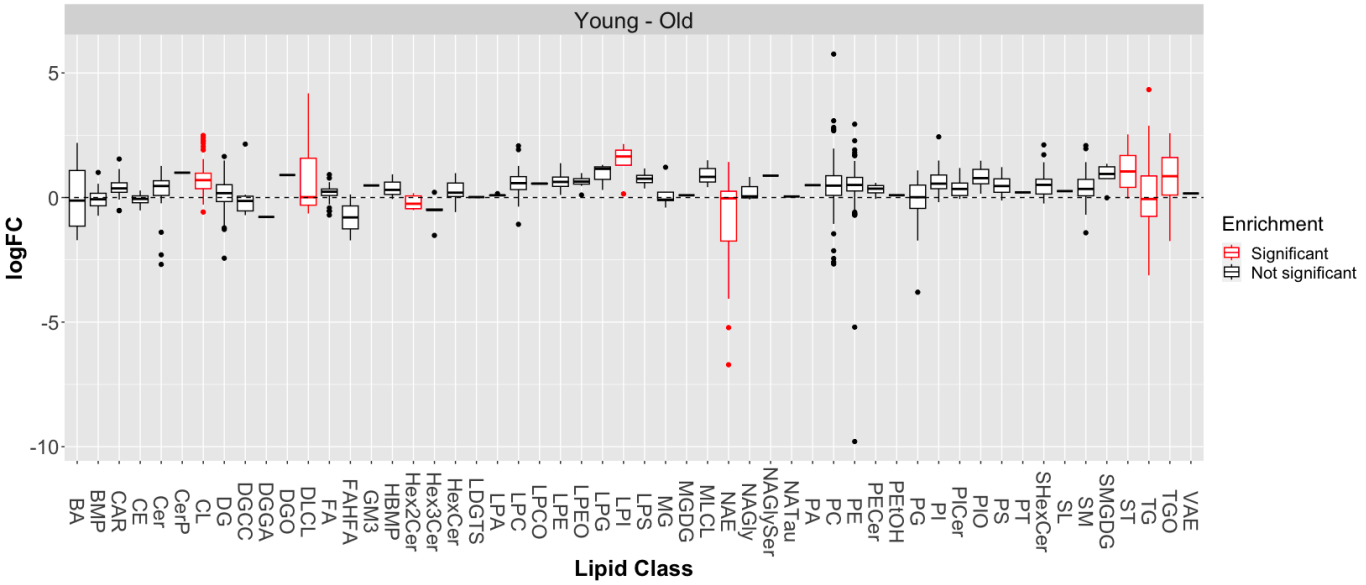
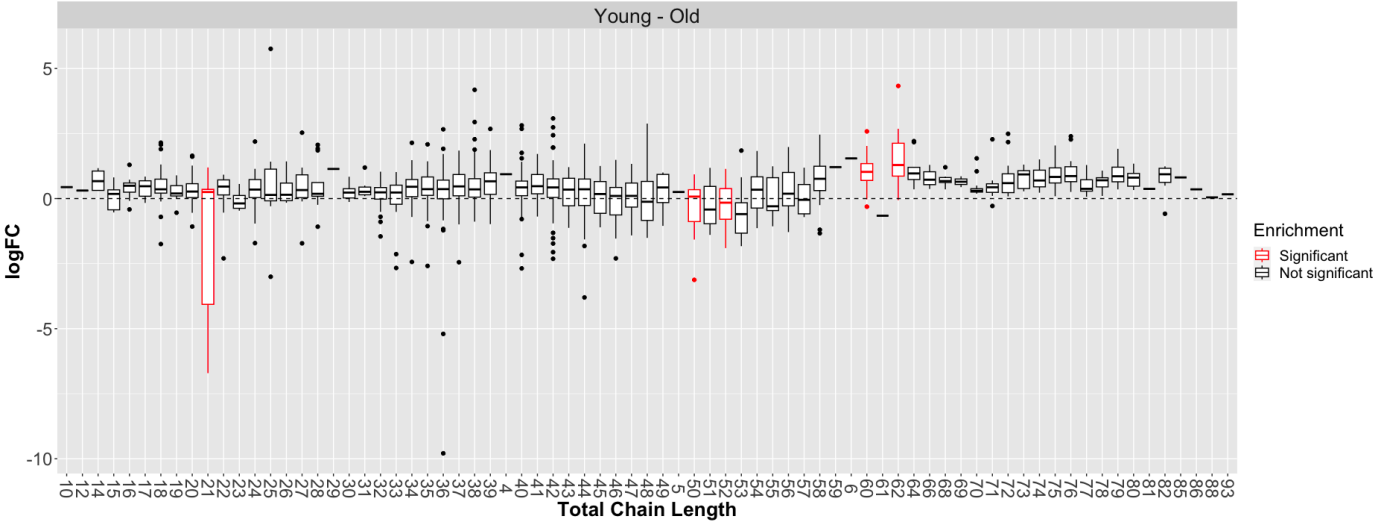
C